Balloon-borne aerosol-cloud interaction studies (BACIS): Field

campaigns to understand and quantify aerosol effects on clouds

4 Ravi Kiran. V[1], Venkat Ratnam. M[1], Masatomo Fujiwara[2], Herman Russchenberg[3], Frank G Wienhold[4],
5 Madhavan. B.L[1], Roja Raman. M[5], Renju Nandan[1], Akhil Raj. S. T[1], Hemanth Kumar. A[1], Ravindra
6 Babu. S[1]

7 [1]National Atmospheric Research Laboratory (NARL), Gadanki, 517 112, India
8 [2]Faculty of Environmental Earth Science, Hokkaido University, Sapporo, 060-0810, Japan
9 [3]Department of Geoscience and Remote Sensing, Delft University of Technology, Delft, 2628CD, The Netherlands
10 [4]Institute of Atmospheric and Climate Science (IAC), Universitaetstrasse 16, Zurich, 8092, Switzerland
11 [5]Department of Physics, Sri Venkateswara University, Tirupati, 517 502, India

14 *Correspondence to*: Ravi Kiran. V (ravikiranv@narl.gov.in)

Abstract.

A better understanding of aerosol-cloud interaction processes is important to quantify the role of clouds and aerosols on the climate system. There have been significant efforts to explain the ways aerosols modulate cloud properties. However, from the observational point of view, it is indeed challenging to observe and/or verify some of these processes because no single instrument or platform is proven sufficient. Discrimination between aerosol and cloud is vital for the quantification of aerosol-cloud interaction. With this motivation, a set of observational field campaigns named Balloon-borne Aerosol Cloud Interaction Studies (BACIS) is proposed and conducted using balloon-borne in-situ measurements in addition to the ground-based (Lidars, MST radar, LAWP, MWR, Ceilometer) and space-borne (CALIPSO) remote sensing instruments from Gadanki (13.45^o N, 79.2^o E), India. So far, 15 campaigns have been conducted as a part of BACIS campaigns from 2017 to 2020. This paper presents the concept of the observational approach, lists the major objectives of the campaigns, describes the instruments deployed and discusses results from selected campaigns. Balloon-borne measurements of aerosol/cloud backscatter ratio, and cloud particle count are qualitatively assessed using the range corrected data from simultaneous observations of ground-based, space-borne lidars.remote sensing instruments. Aerosol/cloud vertical profiles obtained in from the multi-instrumental observations are found similarreasonably agreeing. Apart from this, balloon-borne profiling is found to provides information on clouds missed by ground-based and/or space-borne lidarsmeasurements. A combination of the Compact Optical Backscatter AerosoL Detector (COBALD) and Cloud Particle Sensor (CPS) sonde is employed for the first time in this study to discriminate cloud and aerosol in an in-situ profile. A threshold value of COBALD colour index (CI) for ice clouds is found to be between 18 and 20 and CI values for coarse mode aerosol particles range between 11 and 15. Using the data from balloon measurements, the relationship between cloud and aerosol is quantified for the liquid clouds. A statistically significant slope (aerosol-cloud interaction index) of 0.77 found between aerosol back-scatter and cloud particle count reveals the role of aerosol in the cloud activation process. In a nutshell, the results presented here demonstrate the observational approach to quantifying aerosol-cloud interactions.

1 Introduction

Understanding the fundamental process of aerosol-cloud interactions remains to be a challenging issue in the scientific community, already for more than three decades (Seinfeld et al., 2016). First-ever observational evidence from analysis of ship tracks using satellite imagery had opened up a wide scope for further research in this area (Coakley et al., 1987; Radke et al., 1989). Since then, efforts are underway using different observational and modelling techniques and lead to a significant development in the process-based understanding, quantification, and modelling (Abbott and Cronin, 2021; Fan et al., 2018; Haywood and Boucher, 2000; Koren et al., 2010; Lohmann, 2006; Lohmann and Feichter, 2004; Rosenfeld et al., 2008, 2014b). Despite all these efforts, radiative forcing estimates due to aerosol-cloud interactions both cloud

62 modification and further adjustments (ERFaci) still show large uncertainties (IPCC, 2021) in the range -0.3 to -1.7 W/m^2.

63 Apart from this, climate model simulations have uncertainties because parameterization schemes are inefficient in

64 representing the ways aerosols interact with clouds (Fan et al., 2016; Rosenfeld et al., 2014b; Seinfeld et al., 2016). At the

65 process level, various hypotheses have been proposed after the first indirect effect which was proposed almost four decades

66 ago (Twomey, 1977). All aerosol-cloud effects are found to act specifically to cloud type, background meteorological, and

67 dynamical conditions. For example, the invigoration effect is proposed for convective clouds (Rosenfeld et al., 2014a) under

68 the influence of updrafts. The first indirect effect (Twomey effect) and the second indirect effect (Albrecht effect) for liquid

69 clouds be is influenced by mixing (Costantino and Bréon, 2010), turbulence, and entrainment (Jose et al., 2020; Schmidt et

70 al., 2015; Small et al., 2009). Although the first indirect effect is reasonably well understood, observational limitation poses

71 serious challenges in understanding and/or evaluating other hypotheses.

72 Among the various observational techniques that are currently available (ground-based, space-borne remote

73 sensing, and aircraft or unmanned aerial vehicle; UAV), none of the techniques alone has been proven self-sufficient in

74 aerosol-cloud interaction studies. For example, ground-based (and/or space-borne) lidars suffer serious attenuation and even

75 losses of observations due to the presence of optically thick cloud layers in the atmosphere. Thus, they may not be able to

76 represent the complete vertical structure of clouds and aerosols. Note that information on aerosol/cloud profiles is essential

77 for the estimation of their climate effects. Similarly, satellite data sets have shown distinct results and conclusions

78 (Grosvenor et al., 2018; Koren et al., 2010; McComiskey and Feingold, 2012) using different analytical methods for

79 example changing grid resolutions, etc. Besides this, in-situ measurements using aircraft and UAVs have been remarkable in

80 obtaining detailed information on the microphysics of cloud and aerosol (Corrigan et al., 2008; Girdwood et al., 2020, 2021;

81 Kulkarni et al., 2012; Mamali et al., 2018; Redemann et al., 2020; Weinzierl et al., 2017). However, there are serious

82 limitations concerning altitude coverage, the feasibility of conducting aircraft or UAV campaigns, and the overall cost

83 involved. Also, there is a chance that the aircraft perturb the atmosphere before it measures cloud/aerosol.

84 Thereforeaerosol. Therefore, it is essential to examine the combined information on aerosol/cloud, environmental

85 parameters obtained simultaneously using multi-instrumental techniques. to obtain aerosol, cloud and associated

86 environmental parameters to understand aerosol-cloud interaction.

87   A classic paper by Feingold et al. (2003) first time quantified the 'Twomey effect' using ground-based remote

88   sensing instruments such as a microwave radiometer (MWR), cloud radar, and a Raman Lidar. In an intensive operations

89   program, Feingold et al. (2006) conducted airborne in-situ measurements for obtaining the cloud effective radius using an

90   aircraft in addition to the ground-based and space-borne remote sensing instruments. Pandithurai et al. (2009) also quantified

91   the 'Twomey effect' using a suite of ground-based remote sensing instruments (cloud radar, MWR, polarization Lidar) along

92   with the surface aerosol measurements (aerosol size distribution, scattering coefficient, and cloud condensation nuclei

93   concentration). Similarly, Sena et al. (2016) utilized 14 years of coincident observations from cloud radar and a ~~laser~~

94   Ceilometer along with surface-reaching shortwave radiation measurements from the Atmospheric Radiation Measurement

95   (ARM) program over the Southern Great Plains, USA to investigate aerosol modifications on cloud macroscopic parameters

96   and radiative properties rather than cloud microphysical parameters. In addition to simultaneous measurements of

97   cloud/aerosol, concurrent measurements of thermodynamic and dynamic parameters of the atmosphere are also needed to

98   thoroughly understand the process of aerosol-cloud interactions. A step forward in this direction, McComiskey et al. (2009)

99   used long-term, statistically robust ground-based remote sensing data from Pt. Reyes, California, the USA to not only

100   quantify the 'Twomey effect' but also examine the factors influencing the variability in aerosol indirect effects such as

101   updraft velocity, liquid water path, scale, and resolution of observations. Using a novel dual field of view Raman Lidar and a

102   Doppler Lidar technique, Schmidt et al. (2014) analyzed the data from Leipzig, Germany to explore linkages between

103   aerosol, cloud properties, and the influence of updrafts. Sarna and Russchenberg, (2016) used synergy of measurements from

104   a Lidar (Ceilometer), Radar (cloud radar) and a Radiometer (MWR) collected at ARM Mobile facility at Graciosa Island, the

105   Azores, Portugal, and the Cabaw Experimental Site for Atmospheric Research (CESAR) observatory, The Netherlands, to

106   not only quantify the aerosol indirect effect but also attempted to disentangle the effect of vertical wind (Sarna and

107   Russchenberg, 2017). All these studies contributed significantly to the knowledge on aerosol-cloud interactions but are based

108   on remote sensing techniques, limited to the low-level, warm, and non-precipitating clouds only.

109   Given the measurement limitations discussed above in ground-based multi-instrumental technique, a balloon-borne

110   in-situ measurement is suggested to be the complementary technique as balloons can pass through the cloud (during their

111   ascent/descent) representing the vertical structure of the cloud as well as aerosol below and above the cloud near

112 simultaneously (see Sect. 2 for details) without perturbing the atmosphere. Although there is less information and data on

113 balloon-based aerosol sampling artefacts than on conventional aircraft, information from balloon-borne in-situ measurements

114 in combination with the ground-based and/or space-borne ~~platforms~~remote sensing instruments will be of great help in

115 constructing the complete vertical profiles of aerosol, cloud, and further understanding the process of aerosol-cloud

116 interactions. With this in mind, a balloon-borne field campaign named BACIS (Balloon-borne Aerosol Cloud Interaction

117 Studies) was initiated in the year 2017 at National Atmospheric Research Laboratory (NARL), Gadanki (13.45^{o} N, 79.2^{o} E),

118 India, with the multi-instrumental approach.

119   Balloon-borne measurement of aerosol/cloud was first reported in Rosen and Kjome, 1991 using a backscatter

120 sonde developed by them. COBALD is similar to this but lightweight sonde (Brabec et al., 2012). Measurements of aerosol

121 size distribution in the stratosphere were carried out using an optical particle counter developed at Wyoming university

122 (Deshler et al., 2003). But Smith et al., 2019 developed a novel, low-cost, and lightweight open path configuration optical

123 particle counter, UCASS (Universal Cloud Aerosol Sampling System) for a wide range of particle size measurements

124 covering both aerosol and cloud. Kezoudi et al., 2021 and Mamali et al., 2018 used UCASS and reported balloon-borne in-

125 situ measurement of dust aerosol, ~~and~~ compared UCASS with ground-based~~,~~ and ~~-~~airborne instruments. However, BACIS

126 campaigns are designed to understand and quantify aerosol-cloud interactions. For this, a combination of balloon-borne

127 sondes, COBALD and CPS is used for the first time to separate/discriminate aerosol and cloud in a profile. Note that

128 individually COBALD and CPS have been used in other studies (Brunamonti et al., 2018, 2020; Fujiwara et al., 2016a;

129 Hanumanthu et al., 2020; Inoue et al., 2021; Vernier et al., 2015, 2018).

130   The purpose of this manuscript is to introduce the motivation and objectives of the BACIS Campaigns for

131 quantifying aerosol-cloud interactions. In order to do this, we have discussed most related topics, such as the campaign

132 approach, sensors/instruments employed, analytical methods and comparison of balloon features. Results from selected

133 campaigns focus on discrimination of aerosol/cloud in a profile. Overall, the methods presented in this paper for the data

134 analysis/processing are novel. Using these methods aerosol-cloud interaction is estimated in liquid clouds.

135 **2. Instruments and methods**

136 **2.1. Balloon-borne sensors**

2.1.1. COBALD

The Compact Optical Backscatter AerosoL Detector (COBALD) deployed in BACIS campaigns is a lightweight (540 g) balloon-borne sonde developed in the group of Professor Thomas Peter at ETH Zurich, Switzerland. It is essentially a miniaturized version of the backscatter sonde developed by Rosen and Kjome (1991). A backscatter sonde is a balloon-borne sensor which measures the backscattered light from molecules, aerosol and clouds at ~~multiple~~two wavelengths in the vicinity of the sonde as it passes through the atmospheric column. The COBALD consists of two LED light sources of approximately 500 mW power emitting 455 nm (blue) and 940 nm (termed 'infrared') wavelengths, respectively (Brabec et al., 2012). The light emitted by the sonde illuminates the air in the vicinity, and backscattered light from an ensemble of particles is detected using a silicon photodetector. The emitted beam's divergence (with a full-width half-maximum of 4 degrees), detector field of view (of 6 degrees), and geometrical alignment of optics yields the reception of backscatter light from a distance of 0.5 m (overlapping distance) from the sonde. The region of up to 10 m from the instrument contributes to 90 % of the measured backscattering signal. The real-time backscatter data, in units of counts per second (cps, originating from the internal data treatment) is included in the radiosonde telemetry at a frequency of 1 Hz and sent to the ground station along with the pressure and temperature measurements. In the present case, we have used an iMet radiosonde (InterMet, USA). The COBALD sondes were usually operated for about 15 minutes at the surface (before launch) for thermal stabilization, sonde response is verified by cross-checking the LED brightness monitor signals ~~, and also delivered in counts per second,~~ with sonde specific reference values provided by the manufacturer. The sonde is launched when the ~~return~~ monitor signal data at the surface is within ±15% of the reference value. COBALD sensor illuminates the air in the vicinity. Therefore does not require any flow to operate.

2.1.2. CPS

Cloud Particle Sensor (CPS) sonde is a lightweight balloon-borne sensor (~200 g) developed for the detection of cloud particle number and phase (Fujiwara et al., 2016~~b~~). The latest version of the sonde (launched in the campaigns) is supplied by Meisei Electric Corporation, Japan, along with a Meisei RS-11G radiosonde (Kobayashi et al., 2019; RS-11G(R3) is the model with an interface for CPS). CPS primarily consists of a column (~1 cm x 1 cm in cross-section and ~12 cm in vertical length) for air passage, a diode laser (~790 nm, polarized), and two silicon photodetectors. Cloud particles

162 entering the column due to the balloon ascent are illuminated by the laser. The scattered light from cloud particles is detected

163 by the photodetectors placed at an angle of 55° and 125° to the incident laser light. The detector at 125° comes with an

164 additional polarization plate positioned in front of it for the detection of cross-polarization whereas the detector at 55°

165 measures the intensity of plane-polarized scattered light. The intensities I55 and I125, for the detectors located at 55° and

166 125°, respectively, are provided in voltage, and I55 is related to particle size. The minimum size of a water droplet that can

167 be detected by CPS is found to be 2 µm (1 µm particles are undetected in laboratory experiments using various standard

168 spherical particles) and I55 was found to sometimes saturate (~7.5V) for particles ~80-140 µm (Appendix A of Fujiwara et

169 al., 2016). Real-time data from CPS has been transferred to the ground station through RS-11G (R3) radiosonde at a

170 frequency of 1Hz. CPS data include the number of particles counted in a sec, scatted light intensity (in Voltage) for the two

171 detectors (I55 and I125), as well as particle signal width for the first six particles for each second, and DC output voltage.

172 The particle information is transmitted to the ground station only for the first six particles for each second due to the limited

173 downlink rate of RS-11G which is 25 byte s^{-1}. Before launch, the sonde is tested by spraying water near to air passage

174 column for particle detection. For CPS, the sample flow depends on the balloon ascent rate. Fujiwara et al. 2016, (Appendix

175 B) measured the flow rate within the duct of the CPS by using hot-wire anemometers and estimated that the flow rate in the

176 detection area is about 0.7 times the balloon ascent rate. We used the value of 0.7 (of balloon ascent) for this paper. The flow

177 inside the duct and the detection area would be more or less turbulent, meaning that the flow has a minor component of a

178 complicated function of time and space, but for example, taking a sort of averaging e.g. for 5 seconds, 10 seconds, 1 minute,

179 etc. would dump the impacts of such a turbulent component.

180

181 **2.2. Remote sensing instruments**

182 **2.2.1. MPL/Ceilometer**

183 A Micro Pulse Lidar (MPL) was operated on 076th June and 088th July 2017 during the first two campaigns.

184 Complete technical details of MPL used in the campaign can be found in Cherian et al. (2014). A low energy (< 10 µj) green

185 (532 nm) pulsed laser of pulse width less than 10 ns was shot from MPL at a pulse repetition frequency of 2500 s^{-1}. A

186 Cassegrain type telescope of 150 mm diameter and a PMT have been deployed to collect the backscattered photons (co-

187 polarized) from particles and clouds in the atmosphere. The entire system is operated at a dwell time of 200 ns which would

188 correspond to a range resolution of 30 m. The return signals were collected for 1500 bins which correspond to the total range

189 of 45 km. A profile of backscattered photons was obtained for every 300 μs and all profiles collected were averaged for

190 every one minute. The telescope field of view and laser beam divergence coincide or overlap at above ~150 m. Using the

191 data from MPL (from Gadanki and the nearby location at Sri Venkateswara University, Tirupati, India (13.62^0 N, 79.41^0 E;

192 ~35 km from Gadanki), Ratnam et al. (2018) reported the presence of an elevated aerosol layer in the lower troposphere (~3

193 km) during South-West Monsoon Season and discussed the possible causes for the formation and maintenance of this

194 elevated layer. The low-level jet (LLJ) between 2 and 3 km in the lower troposphere present during the southwest Monsoon

195 causes the formation of an elevated layer. In addition, the presence of shear between LLJ and tropical easterly jet (TEJ)

196 maintains the elevated layer restricting the upliftment of aerosol. Prasad et al. (2019) also used the same dataset to discuss

197 nocturnal, seasonal, and intra-annual variations in the tropospheric aerosol.

198   A Ceilometer (make from Vaisala, Finland) was used in the rest of the campaigns during non-available dates of

199 MPL. It is similar to an MPL but operates at a 910 nm wavelength and provides round-the-clock measurements of cloud

200 base heights, and boundary layer height apart from aerosol extinction under all weather conditions (Wiegner et al., 2014).

201 **2.2.2. Mie Lidar**

202   Mie lidar at Gadanki is a unique lidar system with capabilities to probe the atmosphere to higher altitudes (~30 km).

203 This lidar was operated in almost all the campaigns. A very high energy (600 mJ) pulsed laser with a pulse width of a few 7

204 ns and a pulse repetition frequency of 50 s^{-1} is operated at a wavelength of 532 nm. A 320 mm diameter Cassegrain type

205 telescope along with a couple of PMT has been used as a detection assembly to collect the co and cross-polarized return

206 signal. However, the co-polarization channel (only) is analysed in the present study. The data is stored at a dwell time of 2 μs

207 which corresponds to the range resolution of 300 m and the profiles collected were averaged every 250 sec (~ 4 min). The

208 data is considered to be reliable from an altitude of 3-4 km as the field of view of the Mie telescope and laser beam

209 divergence overlap at this height (Pandit et al., 2014). For the first time, sixteen years of Mie lidar data have been analysed to

210 determine the long-term climatology of tropical cirrus clouds (Pandit et al., 2015). Gupta et al. (2021) reported the long-term

211 observations of aerosol extinction profiles using a combination of MPL, Mie lidar, and a space-borne CALIPSO lidar.

2.2.3. CALIPSO

Cloud-Aerosol Lidar with Orthogonal Polarization (CALIOP) is the space-born lidar onboard the CALIPSO satellite (L'Ecuyer, 2011). CALIOP consists of two pulsed diode lasers operating at 532 and 1064 nm wavelengths with pulse energy of 110 mJ and a repetition rate of ~ 20 Hz. A Backscattered signal is collected by an avalanche photodiode (APD) at 1064 nm and photomultiplier tubes (PMT) at 532 nm. The signals at 532 nm are collected at both parallel and perpendicular to the plane of polarization of the outgoing beam, while for 1064 nm channel polarization is parallel only. The range resolution of the backscattered profile at 532 nm is 30 m for the altitude range from -0.5 to 8.2 km, 60 m for 8.2 to 20.2 km and 180 m for >20-30 km. Horizontal resolution is 0.33 km for -0.5 to 8.2 km and 1 km for 8.5-20.2 km. More details about CALIOP can be found in Winker et al. (2007).

2.2.4. MST Radar

The Indian MST radar located at Gadanki is a high-power coherent backscatter VHF (Very High Frequency) radar operating at 53MHz. A detailed description of MST radar can be found in Rao et al. (1995). Before the BACIS campaign, it has been upgraded to a fully active phased array with dedicated 1 kW solid-state transmitter-receiver units (total power of 1024 kW). This radar operates in Doppler Beam Swinging (DBS) mode to provide wind information covering the troposphere, lower stratosphere and mesosphere. Atmospheric scatterers are advected with the background air motions and the three-dimensional wind velocity vectors (zonal, meridional and vertical) can be directly deduced from the Doppler shifts of the radar echoes received in three independent beam directions. Note that these radars are the only means of getting direct vertical velocities presently and play a crucial role in the understanding of aerosol-cloud interaction processes. For the present study, data is obtained from five beam directions with 256 FFT (Fast Fourier Transform) points and coherent integrations, 4 incoherent integrations, Inter Pulse Period (IPP) of 160 ms, the pulse width of 8 μs coded covering the altitude region of 3 to 21 km with 150 m vertical resolution.

2.3. The observational concept of the BACIS Campaign

236   ~~An observational approach is conceptualized here wherein a balloon-borne in-situ measurement is made~~
237   ~~simultaneously while the multiple remote sensing instruments are operated from the ground and spaceborne platforms.~~ The
238   schematic diagram shown in Figure 1 illustrates the observational approach. A meteorological balloon with specialized
239   sondes such as COBALD (Brabec et al., 2012) and CPS (Fujiwara et al., 2016b) along with a radiosonde is launched ~10-30
240   minutes before CALIOP onboard Cloud-Aerosol Lidar and Infrared Pathfinder Satellite Observation (CALIPSO; Winker et
241   al., 2007) (night time) overpass close by Gadanki. Ground-based remote sensing instruments at NARL, Gadanki such as a
242   Micro Pulse Lidar (MPL; Cherian et al., 2014) and/or a ~~laser~~ Ceilometer (Wiegner et al., 2014), a Mie Lidar (subsequently
243   referenced to as 'Mie'; Pandit et al., 2014), an Indian MST Radar (Rao et al., 1995) and/or a Lower Atmospheric Wind
244   Profiler (LAWP; Srinivasulu et al., 2012) are also operated before, during and after the launch. Other observational facilities
245   such as ambient aerosol instruments at the Indian Climate Observatory Network (ICON), NARL, Gadanki and an MWR are
246   operated during the launch period.

247   Table 1 lists the ensemble of instruments used in the campaign, their purpose and the physical quantity that can be
248   obtained from each instrument. Temporal variation of remote sensing data on the cloud and aerosol profiles is obtained from
249   ground-based (MPL/Mie) lidars. Spaceborne lidar (CALIPSO) also provides the same but for an along-track (roughly
250   meridional) distribution near the time of overpass over Gadanki. ~~On the other hand, i~~In-situ measurements of aerosol and
251   cloud profiles along with background meteorological parameters (temperature, relative humidity, wind speed and direction)
252   are collected using the specialized balloon sounding (COBALD and CPS). ~~Combined data from balloon and~~
253   ~~ground/spaceborne lidar is the basis for the identification of aerosol and cloud particles. Apart from this, t~~Temporal variation
254   in wind components obtained from the ground-based radars (MST Radar and/or LAWP) aids in entangling the effect of
255   vertical winds and turbulence on aerosol-cloud interactions. An MWR provides the cloud liquid water and relative humidity
256   profiles, etc., useful to constrain the cloud water content in a cloud layer to understand the aerosol influence on cloud
257   properties. In addition to these measurements, surface aerosol information obtained by the instrumentation available at the
258   ICON observatory, NARL helps in understanding the role of sources of aerosol from the surface. Altogether, near-
259   simultaneous information on the aerosol, cloud and background meteorological conditions obtained from the multi-
260   instruments is aimed to understand the aerosol-cloud interactions.

261 Initially, when the experiment was being conceptualized, it was thought to conduct a launch once in one or two

262 months. However, due to the limited number stock of specialized sondes (available with us), it was decided to conduct

263 instead two pilot campaigns to demonstrate the concept proposed. Apart from this, it was also required to have

264 balloon/payload tracking equipment to ensure the safe recovery of the payloads. A low-cost GPS/GSM-based tracker is used

265 for theis recovery purpose. Subsequently, tTwo pilot campaigns were conducted in the early hours of 6 June and 8 July 2017.

266 Table 2 lists the date and time of all the balloon campaigns that have been conducted from Gadanki as a part of BACIS

267 campaigns and the instruments operated during the corresponding campaigns. As shown in Table 2, so far 15 launches have

268 been conducted from the year 2017 to 2020.

269 Figure 2 shows the photographs taken at the balloon facility, NARL just before the launch during one of the

270 campaigns. The balloon payload with specialized sondes (COBALD, CPS) and radiosonde (iMet and RS-11G) is shown in

271 Fig. 2(a) and the prelaunch activities at the field are shown in Fig. 2(b). Skilled personnel were deployed for the launch and

272 recovery of the payload. As of now, we have recovered all the launch payloads successfully (except one) with the help of

273 GPS/GSM tracker assembly. Except for the two pilot campaigns, the rest of them were conducted during the night

274 irrespective of the CALIPSO satellite overpass as t There was a maneuverer in CALIPSO orbit during September 2018

275 (CALIPSO track got departed from A-Train to join C-Train. More details can be found at link https://atrain.nasa.gov/),

276 followed by which we could not find CALIPSO nighttime passage close by Gadanki. Apart from this, MPL measurements

277 were not available after a few initial campaigns due to technical issues. However, a laser Ceilometer was operated in place of

278 MPL. Also The other major issue for conducting a campaign there was a the limited availability of specialized

279 sondesSondes, and compatible radiosondes, and GPS/GSM tracker assembly, among others. Because of these reasons, rest of

280 the campaigns were conducted on random dates. However, as seen in Table 2, we have managed to operate all the essential

281 instruments proposed in the observational approach during other campaigns. In particular, the campaigns in the year 2019

282 were conducted once a month (March to June 2019) or for two months (July to December 2019).

283 Figure 2 shows the photographs taken at the balloon facility, NARL just before the launch during one of the

284 campaigns. The balloon payload with specialized sondes (COBALD, CPS) and radiosonde (iMet and RS-11G) is shown in

285 Fig. 2(a) and the prelaunch activities at the field are shown in Fig. 2(b). As shown in fig.2a, the ozonesonde at the centre

serves as the support for the balloon payload. COBALD sonde with a slight upward-looking angle is attached to one side of the ozonesonde and the CPS on another side. Radiosonde (Meisei and iMet) connected to the remaining two sides. All the sondes are tightly packed using adhesive tapes. At the base of the ozone sonde, a wide thick thermocol sheet is arranged to protect the entire payload at the time of ground contact during descent. A couple of GPS/GSM based trackers are also attached to the payload along with a power bank for safe recovery. The entire payload is hung to an inflated balloon with the help of a nylon thread. The length of the thread between the inflated balloon and parachute is 5 m. Similarly, the length of thread between the parachute and payload is 10 m. In this paper, CPS and COBALD data are shown at actual resolution (5 m). But in the estimation of the aerosol-cloud index sensor data is averaged over the thickness of the cloud which is about 300 m. Therefore, the sampling biases would be nullified.

With the observational approach described above, the following scientific issues/objectives are being pursued/realized:

i. Demonstration of the potential of the multi-instrumental observational approach in obtaining the information on the aerosol, cloud, and associated environmental parameters, such as 3D winds, relative humidity, and temperature simultaneously.

ii. Comparison of balloon-borne in-situ measurements among the combination of spaceborne and/or ground-based instruments.

iii. Discrimination of aerosol and cloud in a balloon sounding using the combined observations of COBALD and CPS sondes.

iv. Verifying and quantification of aerosol-cloud interactions and understanding the influence of meteorological and dynamical parameters.

v. Find out the differences, if any, in the estimates of aerosol-cloud interaction using multi-instruments and discuss the possible reasons for discrepancies.

vi. Understanding of how the indirect effects of aerosols change radiative transfer through the atmosphere.

vii. Assessment of Weather and Climate model simulations using the multi-sensor data.

2.4. Methods

2.4.1. COBALD data processing

Backscattered light received by COBALD is contributed by molecules, aerosols and cloud particles in the atmosphere. The molecular Rayleigh contribution to the raw signal (cps) is established during the post-processing of the data using the simultaneous temperature and pressure recordings of the radiosonde. It serves to normalize the total signal in terms of backscattering ratio (BSR) according to

$$BSR = \frac{\beta_{\text{total}}}{\beta_{\text{molecular}}} \qquad (1)$$

Where β_{total} and $\beta_{\text{molecular}}$ are the backscatter coefficients corresponding to the contribution from particles plus molecules and Molecules, respectively. The sole particle contribution is obtained by BSR-1, which expresses the ratio of particle backscatter coefficient to the molecular one. The uncertainty in the COBALD BSR is estimated to be 1% and 5% at the surface level and 10 km, respectively (Brabec et al., 2012; Vernier et al., 2015). The Color Index (CI), referring to the particle backscatter only, is calculated from Equation 2.

$$CI = \frac{BSR_{940} - 1}{BSR_{455} - 1} \qquad (2)$$

By definition, CI is an independent quantity of particle number concentration and is hence useful in interpreting the size of a particle. For analysis, COBALD raw data is binned into 1 hPa pressure levels. This could minimize noise, and unwanted data and smoothen the profile. Figure 3 shows a typical example of COBALD data collected during the second campaign (8 July 2017). BSR at 455 nm and 940 nm wavelength channels are represented by blue and red-coloured lines, respectively, while CI (derived using Equation 2) is shown in the green-coloured line. From Fig. 3, a sharp increase in all parameters (BSR at two channels, CI) found around 5 km associated with a thermal inversion (see temperature profile in Fig.3 in black colour) may be attributed to the presence of a low-level cloud or elevated aerosol layer. Below ~5 km, the BSR profile indicates tropospheric aerosol distribution. Within this altitude, BSR values around 2 km indicate boundary layer confinement. Note no significant changes in CI within this 2 km height. Significant values in all parameters between 10 and 16 km are indicative of multiple high-level cloud layers. In the rest of the campaigns, we have noticed that COBALD has captured profile information that was missing in the lidar data.

2.4.2. CPS data processing

335   The phase of the cloud particle detected by CPS is determined using a quantity called degree of polarization (DOP)

336   given by the following relation:

337                         $DOP = \frac{I55 - I125}{I55 + I125}$ (3)

338   Since the spherical particles (water droplets) do not provide significant voltage in the cross-polarization (I125 close to 0), the

339   DOP values for such particles would be close to 1. On the other hand, the DOP for non-spherical particles (for example ice

340   crystals) would take values between -1 and 1 randomly as I125 is non-zero and may or may not be greater than I55. Apart

341   from this, CPS can also detect the non-spherical particles in the lower troposphere whose DOP values may vary between -1

342   and 1.

343   The volume of the particle detection area within CPS is non-zero and estimated as ~0.5 cm^3 (see section 2.3 of

344   Fujiwara et al., 2016 for details). Therefore, when the particle number concentration is greater than ~2 cm^{-3}, more than one

345   particle would exist simultaneously in the detection area, resulting in particle overlap and multiple scattering and thus a

346   counting loss. The counting loss occurrence can be identified using a housekeeping parameter called 'particle signal width'

347   defined as the time taken for the detection of a single particle. A simple correction of particle count using the particle signal

348   width information is proposed by Fujiwara et al. (2016, see their section 2.3 for the details) using a factor 'f' which is

349   (particle signal width in ms)/(1 ms) as follows. The raw counts from a CPS are corrected for multiple scattering and overlap

350   effects using particle signal width data using Equation 4.

351                         $N_{corr} = N_{meas} \times 4f^3$ (4)

352   Finally, the number of particles counted per second is converted to number concentration by assuming that the airflow at the

353   CPS detection area is 70% of the balloon ascent rate (see Appendices B and C of Fujiwara et al., 2016). The uncertainty of

354   the number concentration when the above correction to the particle count is made (i.e., for the case of > ~2 cm^{-3}) has not

355   been evaluated by Fujiwara et al., 2016. It would be safe to assume that the estimated number concentration is valid in the

356   representation of variations in the cloud property rather than magnitude.

357   CPS data were analyzed at their actual resolution of ~ 5m. Figure 4a shows the corrected cloud particle (number)

358   count (based on eq. 4) for the same day as shown in Figure 3. Significant cloud particle count is found at around 5 km and

359   from above 10 to 16 km. The number of particles counted per second at 5 km turns out to be high suggesting the presence of

360   a dense (optically thick) layer of low-level cloud. The corresponding cloud particle number concentration ($\#/cm^3$) also

361   represents (Fig. 4b) the cloud layers at the same altitudes. The DOP is estimated as per Equation 3. In Fig. 4c, DOP values

362   are found to be clustered in the region close to 1 at ~5 km, indicating that the dense (low) cloud layer is a liquid cloud. On

363   the other hand, the DOP values are randomly distributed between -1 and 1 in the altitude region of >10 to 16 km, indicating

364   that these are ice clouds. In Fig. 4d and 4e, particle signal width is often greater than 1 ms and I55 is sometimes ~7.5 V for

365   the ice cloud region between 11 and 14 km suggesting particle overlap and multiple scattering which might have led to

366   signal saturation. This portion of the profile is more vulnerable to the data correction which has been performed and shown

367   in Fig. 4a.

368   **2.4.3. Lidar data processing**

369   Though the backscattered data at very high altitudes (>30 km) are not significant, it is used as a background signal

370   for noise correction. Range corrected signal (RCS) from MPL/Mie is calculated from noise corrected backscattered signal

371   multiplied with range square. In general, the RCS indicates the intensity of light backscattered from molecules, aerosols and

372   clouds in the atmospheric column. However, inversion techniques are commonly applied to the RCS with an assumption of

373   lidar ratio (the ratio of extinction coefficient to backscattering coefficient) to obtain the profiles of total backscatter

374   coefficient, and extinction coefficient of cloud/aerosol separately. Ground-based lidar data were analyzed at their actual

375   vertical resolutions. However, CALIPSO data were interpolated and processed at every 30 m resolution. This information is

376   used in the discussion (sec 3.1).

377   **2.4.4. Estimation of saturation relative humidity**

378   Two dedicated radiosondes from iMet and Meisei were employed in the balloon campaigns for the measurement of

379   meteorological parameters (temperature, pressure, relative humidity, and horizontal winds with height) as well as to act as an

380   interface with specialized sondes COBALD and CPS, respectively. As mentioned, temperature and pressure profiles from

381   the radiosonde were used in the post-processing of the COBALD sonde to scale the signal to the molecular Rayleigh

382   scattering. In addition to this, radiosonde temperature, and relative humidity is useful in understanding the state of saturation

383   of water vapour in the column. By convention, relative humidity reported from radiosonde is always over the plane surface

384   of liquid water (because radiosonde relative humidity sensors are factory calibrated) even below 0^0C. This is because water

385 droplets may exist even below 0^0C and down to -30 to -40^0C (in the form of supercooled liquid) in the atmosphere.

386 Saturation relative humidity (SRH) is defined in Fujiwara et al. (2016) (see also Fujiwara et al., 2003) as the ratio of

387 saturation vapour pressure over the plane surface of ice (e_{si}) to water (e_{sl}) expressed in units of percentage can be a good

388 metric to describe the state of water vapour in the atmosphere such as sub-saturation, saturation and/or super-saturation in

389 particular at air temperatures below 0^0C (with respect to ice). In this study, both e_{sl} and e_{si} are calculated using Hyland and

390 Wexler formulation (see Appendix A of Murphy and Koop, 2005) by using radiosonde temperature data. For temperatures

391 warmer than 0^0C, water vapour saturation is indicated by 100% RH. For temperatures colder than 0^0C, water vapour is said

392 to be saturated if RH ~= SRH and super-saturated when RH > SRH. This information is used in the discussion (sec 3.2).

393 **2.4.5. Discrimination of cloud and aerosol in a balloon profile**

394 COBALD measurement always represents backscatter light from the combination of aerosol and cloud. Obtaining

395 information on aerosol (only) is not possible (for COBALD) in the presence of clouds, and the corresponding regions have to

396 be identified and rejected. This cloud clearing has been established previously for studies related to the UTLS region

397 (Vernier et al., 2015, 2018). Contrary, for cloud investigation, the COBALD was used in combination with the Cryogenic

398 Frost point Hygrometer (CFH) to identify supersaturation (with respect to ice) below, above and within the cirrus clouds to

399 improve the understanding of microphysical processes in cirrus clouds (Cirisan et al., 2014). This sonde in addition detected

400 volcanic aerosol tracers in the stratosphere (Vernier et al., 2020). The Asian Tropopause Aerosol Layer (ATAL) is a well-

401 documented phenomenon occurring in the UTLS region during the Summer Monsoon Season in South Asia. Vernier et al.

402 (2015) proposed two cloud clearing methods for discrimination of aerosol from cirrus clouds in the ATAL region using the

403 physical quantities Color Index (CI), relative humidity over ice (RHi) and backscatter ratio (BSR) at 940 or 532 nm (the

404 latter was interpolated from the 455 nm data for inter-comparison with CALIOP). In the presence of CFH data, the RHi

405 cloud-filtering approach classifies ATAL/UTLS aerosol layers by the criterion BSR (at 532 nm) < 1.3 and RHi < 70%. For

406 measurements of COBALD alone, the CI method indicates clouds with CI < 7 and BSR (at 940 nm) < 2.5. It was shown that

407 both methods effectively discriminate ATAL aerosol from upper tropospheric thin clouds. Brunamonti et al. (2018) also

408 applied the cloud clearing criteria (BSR at 940 nm < 2.5, CI < 7 and RHi < 70%) following Vernier et al. (2015) and found a

409 clear signal of enhanced BSR (at 455 nm) between 1.04 and 1.12 indicative of the aerosol population in the ATAL region.

410 However, it is noted that the methods proposed by Vernier et al. (2015) and Brunamonti et al., (2018) were developed for the

411 UTLS aerosol and their applicability to COBALD measurements of boundary layer and/or mid-tropospheric aerosol needs to

412 be validated.

413   In the present study, we made use of a CPS sonde in tandem with COBALD. As already mentioned, CPS is

414 sensitive to particles in the size range of >2 μm and hence detects cloud particles (both liquid droplets and ice crystals) and

415 sometimes coarse mode aerosol particles (such as dust) of these sizes. Fujiwara et al. (2016) have demonstrated in detail the

416 potential of a CPS sonde using balloon sounding carried out at mid-latitude (Japan) as well as tropical sites (Indonesia).

417 Narendra Reddy et al. (2018) used a CPS measurement from Gadanki to validate their method of retrieving cloud vertical

418 structures based on radiosonde measurements. Therefore, to better segregate the clouds from aerosols in the COBALD

419 measurements, CPS sonde has added advantage to the methods using simultaneous RH data described by Vernier et al.

420 (2015) and Brunamonti et al. (2018). This implies wherever the cloud is present in a profile, CPS identifies it (along with its

421 phase) and the corresponding COBALD particle backscatter data refers to the cloud. The rest of the particle signals in the

422 COBALD profile should correspond to aerosol. However, it may correspond to the (thin) cloud also which might have been

423 missed or undetected by a CPS. So identification of aerosol and cloud in an altitude profile is the key measurement of this

424 paper. The concept is illustrated in sec 3.2.

425 **2.4.6. Estimation of Aerosol-cloud-interaction Index**

426   Balloon data from all campaigns can be pooled to explore the aerosol-cloud relationship. For this purpose, a simple

427 scheme is developed to carry out the required computations. CPS profile data is looked for a cloud layer present in the

428 altitude regime of liquid or low-level clouds (below 5 km). As already discussed, CPS also identifies particles of non-

429 spherical nature. To separate cloud particles from non-spherical particles, the following conditions have been imposed on

430 various CPS measured parameters. Cloud particle count should be >10 #/s, cloud droplet number concentration >10^{-3}#/cc,

431 DOP>0.6, relative humidity >95% and temperature >0 degC. As there is a chance of randomly distributed data points in the

432 measurement column satisfying the above conditions, we considered only those points present continuously up to a thickness

433 minimum of 100 m (with at least one point for every 40 m). Further, COBALD data of blue backscatter 100m, 200m, 300m,

434 400m and 500m below the cloud base has been picked up separately (for the same profile) as a proxy of aerosol to check its

435 influence on the cloud above. As already mentioned, post-processed data of backscatter ratio from COBALD sonde

436 represents the contribution from both molecule and particle (cloud and/or aerosol). Hence, the particle backscatter ratio is

437 obtained by subtracting the backscatter ratio from one. To avoid high values of particle (blue) backscatter ratio possibly

438 originating from the interaction with high relative humidity usually expected near to cloud base (boundaries), we have

439 adopted two methods. First, high values of particle (blue) backscatter below the cloud base are removed if beyond a

440 threshold value of 3.15. The threshold is arrived at using a box plot (figure not shown) drawn for all the particle backscatter

441 data set (for sounding with clouds) from cloud base to 500 m below and found that 3.15 corresponds to the upper whisker

442 (Q3+1.5*(Q3-Q1)). Further, the particle backscatter data is corrected for relative humidity in case a statistically significant

443 (p-value <=0.05) and good correlation (>0.71) is found among relative humidity and particle backscatter ratio. A typical

444 example from the scheme is shown in Fig. 5 for the launch conducted on 01 November 2018 which depicts cloud layers,

445 blue particle backscatter ratio below the cloud along with shaded black dots (representative of aerosol backscatter ratio). The

446 scheme is applied to the balloon sounding and the results were discussed in sec 3.4.

447 Aerosol-cloud interaction can be quantified based on an index (ACI) using three methods discussed in Feingold et

448 al., 2003, 2006. ACI is defined as the slope of the linear fit between the logarithm of cloud proxies such as cloud optical

449 depth, cloud particle radius and cloud droplet number with the logarithm of aerosol proxy. ACI in this study has been

450 estimated using the equation (5).

451
$$ACI = \frac{dlogNc}{dlogBSRb} \qquad (5)$$

452 Where cloud droplet number count (Nc) is taken as cloud proxy whereas COBALD (blue) particle backscatter is (BSRb)

453 taken as aerosol proxy. It is to be noted that cloud particle number concentration is used here to represent cloud property

454 instead of droplet number concentration as the former is a direct measurement (of CPS). The slope of the linear fit between

455 the natural logarithm of Nc and BSRb indicates the magnitude of the aerosol-cloud interaction (ACI index) which should be

456 between 0 and 1 (Feingold et al., 2003). Note the condition shown in eq.5 is independent of the liquid water path as it

457 verifies/quantifies the aerosol activation process.

458 **2.4.7. Uncertainty in ACI estimation**

459   The uncertainty in ACI stems from both uncertainties in the COBALD backscatter ratio and CPS cloud particle

460   counts. The slope of the curve (linear fit of data on a log-log scale) can be written as a function of BSRb (blue backscatter

461   ratio) and Nc (cloud particle count) as,

$$ACI = f(BSRb, Nc) = \frac{LogNc - C}{LogBSRb} \quad (6)$$

463   Where 'C' is the intercept of the curve. The partial derivative of *f(BSRb, Nc)* indicates uncertainty in ACI with respect to

464   uncertainty in individual parameters (Nc and BSRb). The combined uncertainty (UC) in ACI is given by the equation,

$$UC = \sqrt{(\frac{\partial f(BSRb, Nc)}{\partial BSRb})^2 (uBSRb)^2 + (\frac{\partial f(BSRb, Nc)}{\partial Nc})^2 (uNc)^2} \quad (7)$$

466   Where *uBSRb* and *uNc* are individual uncertainties.

467   **3. Results**

468   **3.1. Comparison of balloon measurements**

469   It is important to know the performance of these sondes in comparison to other measurement techniques. Here, we

470   make use of data from two pilot campaigns to demonstrate the consistency of balloon-borne measurements with that of

471   ground-based and spaceborne remote-sensing instruments. As mentioned previously, the first two (pilot) campaigns have

472   been conducted in line with the proposed concept.

473   **3.1.1. Pilot campaign-1 (launch held on 06 June 2017 at 01:50 LT)**

474   The CALIPSO satellite overpass time for the first pilot campaign was around 02:00 LT on 06 June 2017 (starting

475   time of the track). The balloon was launched at 01:50 LT on the same day just before CALIPSO overpass time. Combined

476   measurements from specialized balloon-borne sondes and ground-based and space-borne lidars obtained during the first

477   launch of the campaign are shown in Figure 6.

478   The BSR from COBALD sonde at 455 nm (950 nm) is plotted in Fig. 6d as a blue (red) line. BSR from both

479   channels is referenced to the same x-axis scale. Similarly, cloud particle number concentration (dN, #/cc) from CPS sonde is

480   plotted as black dots (Fig.6e). On the other hand, range corrected signal (RCS) from ground-based lidars (Mie, MPL) is

481   averaged over a short period during the CALIPSO overpass and plotted in magenta (averaged from 01:50 to 02:00LT),

482   orange colour lines (averaged from 01:50 to 01:55 LT), respectively (Fig.6f). The total attenuated backscatter (km^{-1} sr^{-1})

483   from CALIPSO is also averaged for the profiles found nearest to the location and shown in an olive green colour line

484 (Fig.6f). The significant peaks in physical quantities being compared among the different measurements are representative of

485 responses from clouds and aerosols in the atmosphere. At this point of discussion, we have not distinguished their

486 contributions. The balloon drifts away from the launch location with time, therefore, it is also required to check the degree of

487 co-location of measurements with the lidars. To facilitate this, a portion of nocturnal variation (representing the balloon

488 launch duration) in range corrected signal from both Mie and MPL is shown in Fig. 6b and 6c, respectively. The CALIPSO

489 overpass track consisting of 166 profiles is also plotted as a function of longitude (Fig. 6a). For the sake of easy

490 identification of simultaneous lidar measurements, the balloon indices such as height and drift (radial distance from launch

491 location) are overplotted as a function of time on contour maps as shown in black and red-coloured lines, respectively (Fig.

492 6b and 6c).

493 Balloon-borne in-situ measurements from COBALD and CPS show significant peaks in the lower tropospheric

494 (below 4 km) and upper troposphere (between 13 and 17 km) at the same altitude regions. It can be seen from Fig. 6d and 6c,

495 that there is a good resemblance between the in-situ and MPL measurements in the lower tropospheric (below 4km). This is

496 because almost no change in the atmospheric conditions as the balloon took approximately 15 minutes to reach an altitude of

497 4 km with a radial distance of 5 km away from the launch location. Mie lidar information is not reliable for this altitude

498 region (below 4 km) as it is not in the overlapping region of the telescope viewing geometry and laser beam dispersion (see

499 section 2). CALIPSO signal also looks to be dispersed and noisy for this altitude region. This could be due to the attenuation

500 of the signal from the top side layers as seen in Fig. 6a at a longitude of 79.24^o E (nearest profiles longitude).

501 Next to this is the sharp peak seen in COBALD red channel at slightly below 9 km (Fig. 6d). This again can be seen

502 in Mie and MPL profiles also (Fig. 6b, 6c) but at 8.4 km (slightly below cloud detection height). However, it is to be noted

503 that these profiles are averaged for a short duration of time during the CALIPSO overpass. There is another peak in the Mie

504 lidar profiles at ~7.2 km (Fig. 6b), which is not seen in COBALD. It is approximately 45 min (around 02:45 LT) from the

505 time of launch when the balloon reached the altitude of ~9 km and 5.8 km away before detecting a sharp peak. As there is no

506 significant range corrected signal during this time and altitude in the ground-based lidar data (Fig. 6b and 6c), the sharp layer

507 detected by COBALD may be a localized cloud layer or a passing layer which might have ascended/descended. Exact

508 attribution can be made with a detailed study but it is beyond the scope of the current analysis.

509   Further, the balloon drift was within a 10 km range until 03:00 LT when it reached heights of ~12 km. This implies

510   weak horizontal winds and thus weakly associated wind drifts as well. Thereafter, the balloon started drifting rapidly due to

511   high wind speeds between 10 and 20 m/s. Both the in-situ measurements of COBALD and CPS show strong double peaks

512   from ~13-15.5 km and 16-16.5 km (Fig. 6d, e). Profiles from Mie, MPL and CALIPSO also showed similar peaks except for

513   MPL for which the upper side peak is missing (Fig. 6f). It may be once again noted that these profiles are averaged for a

514   short duration of time during the CALIPSO overpass the and return signal from MPL at high altitudes (~16 km) during the

515   same time suffered severely due to the presence of a mid-tropospheric cloud layer (at ~7 km) as seen in Fig. 6c. This is not

516   the case for the return signal from Mie Lidar as the power and energy of the Mie laser are relatively high (Fig. 6b). However,

517   strong double peak structures can be noticeable in the simultaneous observations of both ground-based lidars (Mie and MPL)

518   at similar heights during the time corresponding to the balloon altitude of 13 km (post 03:00 LT). Therefore, the same upper

519   tropospheric cloud layers detected in the ground, spaceborne and in-situ measurements suggest they are extended cloud

520   layers. Dynamical aspects of the southwest monsoon over the sub-continent refer to the presence of Tropical Easterly Jet

521   (TEJ) which is strong enough to swipe anvil clouds of mesoscale convective systems to thousands of kilometres

522   (Sathiyamoorthy et al., 2013).

523   **3.1.2. Pilot campaign -2 (launch held on 08 July 2017 at 01:35 LT)**

524   The starting time of the CALIPSO overpass track for the second pilot campaign was at 02:00 LT. The balloon was

525   launched at 01:35 LT nearly 30 minutes before the starting time of the CALIPSO overpass. Data from all the instruments are

526   plotted in Figure 7, which is prepared the same as Figure 6. MPL and Mie profiles were averaged from 01:50 to 02:00 LT

527   (close to the CALIPSO overpass time over Gadanki).

528   The observations from COBALD and CPS are matching reasonably well (Fig. 7d, e) as significant peaks were

529   found in the lower troposphere (0-5km) and upper troposphere (10-16 km). The profiles from spaceborne and ground-based

530   lidars (Fig. 7f) also show a similar response as in-situ measurements (both in the lower and upper troposphere) except that

531   lidar measurements exhibit additional peaks in the mid-troposphere (between 5 and 10 km). It is to be noted that profiles

532   from lidar measurements are averaged over a short period, as mentioned before.

533   Simultaneous observations from both the spaceborne (CALIPSO) and ground-based (Mie and MPL) lidars are

534   shown in Fig. 7 a, b &c respectively. Due to high wind speeds (10-20 m/s) the balloon drifted about 5 km away from the

535   launch site while crossing boundary layer height (~2km). The features found within the boundary layer as measured by in-

536   situ instruments (Fig. 7d) are in agreement with that of MPL measurements (Fig. 7c) for the same altitude region. Note that,

537   Mie lidar measurements are not reliable at these low altitudes and CALIPSO has not yet started passing by the launch site.

538   The balloon continued to drift away but with a reduced wind speed of 10 m/s. At around 4.3 and 4.7 km (10 km away from

539   the launch site), the balloon detected two layers (strong peaks). The time corresponding to this balloon height was around

540   01:50 LT and at this point, two layers can also be seen in both the ground-based lidars at the same altitudes (Fig. 7b and c)

541   indicating the presence of an extended layer (evident in both the in-situ and ground-based measurements). The layer at 4.7

542   km was also noticeable in the CALIPSO profile measurements (Fig. 7a). This is because the CALIPSO started coming close

543   to the site when the balloon was at this height and the CALIPSO profile corresponds to an average of (nearest) profiles at

544   around 79.32^0 E longitude (Fig. 7a). Further, the balloon started drifting towards the launch site until it reached a height of

545   ~7.5 km at a distance of ~13 km away. While moving towards the site, the balloon started detecting the layers starting from

546   11 km. The time corresponding to the balloon height of 11 km is around 02:45 LT and at this point of time simultaneous

547   MPL data show almost weak returns (Fig. 7c), whereas Mie lidar shows a better return signal (Fig. 7b) than MPL. In

548   continuation of this, the balloon started drifting further toward the site until it reached as close as ~3.5 km at a height of

549   ~12.5 km. Thereafter, it started moving rapidly away from the location with high wind speeds due to the characteristic of

550   TEJ. Multiple layers of clouds have been nicely captured by in-situ measurements from 11 km to ~ 16 km. However,

551   prominent lidar returns were not noticeable in the simultaneous observations of Mie and MPL. This is because of a strong

552   lower tropospheric cloud layer present at around 5 km limiting the detection of upper tropospheric cloud layers by both

553   ground-based lidars. However, all these layers were prominently captured in CALIPSO observations as it is top-down laser

554   probing.

555   In summary, the data from both pilot campaigns illustrate the limitations of the ground-based and/or spaceborne

556   lidars in detecting the complete cloud vertical structure. At the same time, in-situ data emphasize reasonable agreement of

the balloon-borne measurement with the ground-based as well as space-borne measurements and add to the remote sensing techniques while detecting the missing portion of the cloud vertical structure.

The observational facilities at NARL are shown in figure 8. A typical example of high-resolution vertical wind measurements obtained from MST Radar on 8 July 2017 is shown in Figure 89(f) and profiles of all the three-dimensional winds averaged between 02:30 LT to 03:30 LT are shown in Figures 89(a)-(c) to compare the wind measurements. We also superimpose the zonal and meridional winds in the respective panels obtained from radiosonde for comparison. Consistency in the measured winds in these two independent techniques can be noticed. Since this campaign falls during the Indian Summer Monsoon season, easterly wind velocities exceeding 50 m/s, which is called TEJ, can be noticed between 14-16 km altitudes as a part of synoptic-scale systems (Fig. 89a). In addition, zonal winds are westerly, which is also part of a large-scale monsoon system. These winds play a crucial role in bringing clouds and aerosol from far away sources. In general, meridional winds are weaker and most southerly (Fig. 89b). Vertical winds show mostly updrafts, except in the UTLS region where downdrafts are noticed (Fig. 89c) and similar features persist through this campaign (Fig.89f). Occasional patches of updrafts and downdrafts can be noticed during the campaign, which is associated with monsoon convection. These vertical winds act in the upliftment of aerosol and clouds. Enhanced SNR layers are also noticed (Fig. 89d) at a few altitudes mostly related to large temperatures and water vapour gradients generally occur in the presence of clouds. Doppler width (Fig. 89e) shows higher values below the boundary layer and UTLS region suggesting active turbulence.

3.2. Interpretation of aerosol and cloud features in a balloon profile

To fulfilfulfill the primary objectives of the campaign, it is a priority to distinguish aerosol and cloud in a balloon-borne in-situ profile. In connection with this, combined measurements of CPS and COBALD from a balloon sounding held on 27 June 2019 at 23:30 LT are interpreted as shown in Figure 910. This particular sounding is selected because it showcases all the features that can be detectable by a CPS sonde in a profile such as liquid cloud, supercooled liquid cloud, ice cloud, and non-spherical particle layers. INSAT3D brightness temperature shown in Figure S1 indicates the evolution of a localized cloud system north of the observational site initiated a few hours before the launch and eventually spreading over the site.

581   To characterize the background conditions of the atmosphere, meteorological parameters such as relative humidity

582   (RH), and temperature (T) obtained from RS-11G radiosonde are plotted in Fig. 910a (wine red and blue colour lines). In

583   Fig. 910a, SRH is also shown (in yellow colour). The SRH and RH can be read from the same top-X scale in wine red colour

584   as shown in Fig. 910a.

585   The CPS sonde usually features clouds that can be better identified with the information based on DOP, and

586   corresponding profiles of T, RH, and SRH. From Fig. 910d, DOP values close to 1 (from 0.6 to 1) are noticeable at different

587   altitude ranges in the profile viz., 3.5 to 5.5 km, 8.6 to 9 km and DOP values spread (-1 to 1) between 9 and 11 km. In the

588   altitude range from 3.5 to 5.5 km, CPS detected multiple liquid cloud layers, corresponding to the multiple layers of 100%

589   RH. However, the corresponding COBALD blue and red backscatter data points are limited (Fig. 910b). This is because

590   COBALD backscattered signals showed missing values due to saturation of photodiodes in the presence of thick liquid cloud

591   layers and that had to be removed during post-processing of data and are not discussed further.

592   The layer extending between 3.5 and 3.8 km (300 m thick) is observed with RH and T in the range 99-100% and 7-

593   8.7^0C, respectively, indicating saturation of water vapour with respect to liquid (RH~=SRH) which is conducive to the

594   formation of a (liquid) cloud. Further, the majority of droplet number concentrations in this liquid cloud layer range between

595   0.1 to 1 #/cm^3. A rough estimate of particle size information (water droplet or ice crystal) can be inferred from CPS voltage

596   data (I55). According to Fujiwara et al. (2016), I55 mostly lying below 1V suggests these droplets are sized ~2-13 μm.

597   Another liquid cloud layer extending from 4 to 4.4 km (400 m thick) is observed with vapour saturation over liquid (100%

598   RH) and temperatures from 3-6^0C. CPS shows that droplet number concentration peaks in the range 0.1-10 #/cm^3 with the

599   highest in 0.1-1 #/cm^3. The intensity (I55) values (<1 V) indicate the majority of droplet sizes are ~2-13 μm. The third liquid

600   layer in the range of 3.5 to 5.5 km is observed between 5.1-5.5 km (400 m thick) with the highest droplet number

601   concentrations in the range of 0.1-10 #/cm^3, sized around 2-13 μm (I55<1 V). However, RH observations show 100%RH or

602   RH>SRH ie. water vapour super-saturated over ice at temperatures slightly below 0^0C (0 to -3^0C), suggesting that the cloud

603   layer may be composed of supercooled liquid droplets. Another clear supercooled cloud layer was detected between 8.6 and

604   9 km (400 m thick) with super-saturation of vapour over ice at 100%RH or RH>SRH and -21.5 to -23.5^0C temperatures. The

605   observed features of droplet number concentration and particle size are similar to those of the supercooled cloud found in the

606 lower atmosphere. The only difference that could be noticeable is in the distribution of DOP values as shown in Figure S2,

607 which indicates the tendency of droplets toward non-sphericity in the mid-tropospheric supercooled liquid cloud. COBALD

608 signals were found limited for all liquid/supercooled layers discussed above.

609   The topmost layer in the upper troposphere spreading from 9.5-11 km is an ice cloud layer as per its DOP values.

610 The temperatures within the cloud are found in the range of -22 to -40^0C. RH values are >SRH, suggesting the super-

611 saturation of vapour (over ice) within the ice cloud. The histogram of data for all the parameters obtained from COBALD

612 and CPS for this ice cloud layer (9-11 km) is shown in Figure 11~~0~~. The number concentration of ice cloud particles (Fig.

613 11~~0~~a) lies between 0.01 to 10 #/cm^3 with a peak in the range of 0.1-1 #/cm^3. Non-sphericity of particles is seen by the wide

614 distribution of DOP values in the range -0.4 to 1 with the majority of them lying close to 0 (Fig. 11~~0~~b). In particular, DOP

615 values close to 0 indicate (see section. 2) that both plane and cross-polarization intensities of scattered light (I55 and I125)

616 are comparable. This happens when both detectors get saturated due to a large number of small size particles and/or a few

617 large-sized ice particles or both. In support of this, the I55 values (Fig. 11~~0~~c) are found to peak in the 7-8 V range (~7.5 V)

618 for such cases. Further, if saturation voltages are due to large size then they may correspond to ~80-140 μm or greater ice

619 particles (corresponding to I55 of ~7.5V), assuming that the results from laboratory experiments by Fujiwara et al. (2016)

620 using standard spherical particles can be applied for these ice clouds. Apart from this, the second peak in I55 noticed below

621 1V corresponds to ice particles roughly sized between 2 and 14 μm.

622   The COBALD BSR corresponding to this ice cloud is symmetrically distributed from 1-10 and 10-100 for blue

623 (Fig. 11~~0~~d), red (Fig. 11~~0~~e) wavelengths, respectively. However, there are some observations which are beyond 10(100) at

624 blue (red) wavelengths. Similarly, the CI for this cloud (Fig. 11~~0~~f) is found mostly between 10 and 20 but for a few

625 instances, it is observed from 20 to 40. From the definition (see section 2), the CI is independent of the number concentration

626 hence it can be used as an indicator of the mode radius of particles. With the assumption of the single-mode log-normal size

627 distribution of spherical aerosol/cloud particles, Mie calculations show CI is 4-10 for small particles of mode radius up to 1-2

628 μm and 14-20 for large particles of 2-20 μm. CI converges to around 20 as a geometric limit for very large particles of mode

629 radius > ~50 μm. However, CI can have values >20 at mode radius 2-20 μm as CI is a non-monotonous function of mode

630 radius and exhibits Mie oscillations (due to variations of scattering efficiencies with size parameter). The amplitude and

631   frequencies of Mie oscillations depend on the width of the log-normal size distribution assumed. At a width higher than say

632   2 (representing polydisperse aerosol populations), these oscillations are mitigated and lead to a monotonous dependency of

633   CI and mode radius. For stratospheric aerosols in the size range of 0.02-0.4 µm, the CI is found to be in the range of 5-7

634   (Rosen and Kjome, 1991). This is because stratospheric aerosols exhibit size distributions with narrow standard deviations.

635   Aerosol size distributions in the UTLS region may also be assumed as log-normal (similar to stratospheric aerosols) hence

636   the criteria CI<7 might have suited for cloud filtering in the ATAL region (see Section 2). For the present case of the ice

637   cloud layer (9-11km) discussed above, CPS indicates the presence of small (2-14 µm) and very large ice particles (>80 µm).

638   So, the standard deviation of log-normal size distribution in the cloud layer of large particle mode must be wider. Therefore,

639   Mie oscillations may be expected to be at a minimum. Probably because of this, the majority of CI values for the cloud layer

640   are found between 15 and 20, which may correspond to a mode radius of > ~50 µm (geometric limit). It may also be

641   concluded that the CI of 20-40 (with very few values >30) corresponds to small particles of mode radius > 2-20 µm (due to

642   Mie oscillations). COBALD size interpretations (based on CI) are in support of CPS-based size interpretations. Since the

643   majority of CI falls between 15 and 20, the I55 of ~7.5V in CPS would have been caused by large size particles.

644   In the lower troposphere up to 2 km where water vapour is well sub-saturated (50-70 %RH), CPS also shows

645   particle signals (Fig. 910c). The DOP values range from -0.4 to 1 but with lower number concentrations (0.001-0.01 #/cm^3)

646   and less than 1 V of backscatter intensity (I55), indicating these particles as non-spherical in shape similar to the ice cloud

647   particles. Since it is not possible to have ice cloud particles at these lower altitudes in dry conditions (RH<70%), it may be

648   possible that these particles are coarse mode non-spherical aerosol particles. COBALD observations indicate a CI of 11-12.

649   Thus, both the COBALD and CPS observations indicate aerosol may be of size ~2-5 µm. To investigate the possible origin

650   of these coarse mode aerosol particles, Hysplit 7-day back trajectories for 5 days before and after the date of launch are

651   calculated and shown in Figure S3 (in different colour lines). These Hysplit back trajectories (Stein et al., 2015) indicate the

652   air parcel pathways ending at every 1 km altitude from 1 to 5 km over Gadanki at the time of balloon launch (18 UTC). It

653   can be seen (from Fig. S3) that, the air masses originated from the Indian Ocean passing through the Arabian Sea before

654   reaching the Gadanki location for heights of 1 to 3 km. Therefore, the air masses were of marine origin, and the particles

655   were possibly coarse-mode water-soluble particles (such as sea salt) which can grow hygroscopically due to the availability

656 of moisture over the Ocean surface (Mishra et al., 2010; Ratnam et al., 2018). The rainwater chemical analysis reported by

657 Jain et al. (2019) at Gadanki supports this conclusion as they found dominance of water-soluble ions during the southwest

658 monsoon (June to September). Above 3 km altitude, the air masses are coming from the Saharan desert region (within 7

659 days) which may bring non-spherical coarse mode dust particles to the launch location (Mishra et al., 2010). Thus, in the

660 case of lower tropospheric coarse mode aerosol (water-soluble aerosol particles), the CI can be >7 at RH<70%.

661 In the altitudes of 6-8.5 km (Fig. 910), CPS has detected no cloud. However, COBALD data shows, that CI values

662 ranging from 3-8 in the altitude range of 6-7 km and 3-12 in the altitude range of 7-8.5 km may indicate the presence of

663 aerosol particles undetectable by a CPS (i.e., of sizes <2 μm). RH values indicate sub-saturated conditions throughout this

664 altitude region. However, between 7 and 8.5 km, RH increases and becomes greater than the ice saturation RH values

665 (saturation with ice). Corresponding to this RH change, CI, as well as red channel BSR, is also found to increase. This

666 suggests the growth of small aerosol particles under high humidity conditions until the RH approaches ice saturation where

667 supercooled liquid droplets are observed (8.6-9 km) in CPS whose features have been discussed already. Since the COBALD

668 CI values are mostly <10 in this altitude range, the majority of particles detected might be sized up to 1-2 μm.

669 **3.3. Statistics on COBALD colour index**

670 To generalize the optical properties specific to aerosol and cloud, combined data from COBALD and CPS (from

671 multiple launches) has been investigated in detail. The liquid/supercooled cloud, ice cloud and non-spherical particle layer

672 depth are carefully identified with the help of DOP data from CPS (discussed in Section 2). The corresponding data of

673 temperature, relative humidity, BSR, CI, and peak particle number concentration have been picked up for estimating

674 statistics. Further, threshold values of COBALD parameters were tried to identify for the said categories of aerosol and cloud

675 cases. Among 15 balloon soundings, those soundings were considered where CPS detected cloud particles and both blue and

676 red channel data are not missing from COBALD. With these conditions, 8 balloon soundings were identified for estimating

677 statistics.

678 Table 3 shows the mean (median) values of CI and other parameters corresponding to the ice cloud layers from 7

679 launches. Fig. 121(a) shows the complete statistics of CI in the form of a box plot for the same ice cloud layers. Fig. 121(b)

680 shows a histogram of CI from each campaign indicated by different colours. From Table 3, ice clouds are seen above 9 km

681   with temperatures colder than -20^{0}C. For example, an ice cloud layer was found between 9.3 to 16 km on 30 April 2019 with

682   temperatures in the range of -22 to -79^{0}C, RH close to SRH and mean (median) value of CI is 19.4 (19.3), BSR is 16.4 (8.6)

683   at 455 nm, 302 (147) at 940 nm, peak droplet concentration is in the range 10^{-1} to 1#/cc. Similarly, from Table 3, the range of

684   mean (median) values of BSR is noticed to be from 1.6 (1.4) to 17.2 (17.5) and 12.2 (8.7) to 318 (313) at 455 and 940 nm,

685   respectively. Therefore, it is difficult to arrive at threshold values of BSR for ice clouds based on Table 3. This may be partly

686   because BSR depends not only on the particle number concentration but also the size. However, it is interesting to note

687   (except for a few cases in Table 3) that BSR data of ice clouds (at both channels) tend to be greater for densely populated

688   clouds. On the other hand, the difference between mean and median values of CI is not large, thus not much variance in CI

689   within the ice cloud. It is also clear from Table 3 and Fig. 12̶1̶(a) that about 90-95 percentile of CI values of ice clouds are

690   above 15 and below 25 with mean/median values in the range 18-20. The same is also seen in the histogram of CI shown

691   (Fig. 12̶1̶b) in different colours for different sounding dates where a greater number of points in a sounding are lying close to

692   20. Therefore, it may be concluded that the mean value of CI of ice clouds would be between 18 and 20.

693   The data from 8 soundings are also analysed for CI (and other parameters) of liquid clouds. However, it is noted

694   that liquid clouds were not observed as often as ice clouds in the balloon data. In the second campaign (8 July 2017) a liquid

695   cloud layer was observed at altitudes from 4.7 to 4.86 km (160 m) with RH>SRH, temperatures in the range of -0.4 to -

696   1.65^{0}C. The mean value of CI corresponding to this liquid cloud layer is very high around 50. Similarly, another liquid cloud

697   layer was observed in the fourth campaign (01 Nov. 2018) in the altitude range of 2-2.3 km (300 m). The corresponding CI

698   values are high and above 100 (up to 200). A couple of thin supercooled liquid cloud layers were also identified on the same

699   sounding between 6.1-6.17 km (7 m) and 6.6-6.8 km (200 m). The corresponding CI values are found with mean (median)

700   values of 19.5 (19.4) and 32.6 (32.8), respectively. Apart from this, a strong boundary layer (liquid) cloud layer was

701   observed on 23 Mar. 2019 (fifth campaign) between 0.9 and 1.2 km (300 m). The corresponding CI of liquid cloud was

702   found to be high with mean, and median values of 60-80. From the above discussion (including the liquid cloud cases not

703   discussed above), it is noticed that the CI for liquid clouds is high. The difference in CI values of liquid clouds can be

704   attributed to the thickness of the cloud, and the density and droplet size of liquid clouds.

705   Non-spherical large dust aerosol particles were identified by DOP values from CPS in the lower troposphere where

706   RH is far less than 100%. Statistics on COBLAD CI (and other parameters) for these non-spherical particle cases are

707   presented in Table 4 using the data from 8 soundings. For example, a non-spherical particle layer was found between 0.5 and

708   2.5 km altitudes on 06 June 2017 with temperatures in the range of 15.5 to 27.6^0C and relative humidity is dry from 63.5 to

709   81.3%. The mean (median) value of CI corresponding to this non-spherical particle layer is 12.3 (12.5), BSR is 1.45 (1.4) at

710   455 nm, 6.5(6) at 940 nm and peak particle concentration is between 10^{-3} and 10^{-1} #/cm^3. The peak particle concentration of

711   all non-spherical layers is found to be in the same range and hence not shown. From Table 4, it can be noticed that the non-

712   spherical particle (aerosol) layer is found from the near-surface to the 5 km altitude depending on the month or season.

713   During the monsoon season (font in blue colour in Table 4), non-spherical particle layers were observed mostly from the

714   near-surface (500m) to 2.5 km whereas during pre-monsoon (font in wine red colour) it is found from 0.5 up to 5 km. The

715   reason for the difference in layer thickness among seasons may be attributed to the mixing within the lower troposphere,

716   long-range transport and local sources. Since these layers are confined mostly to the lower troposphere, the temperatures are

717   in the range of 27 to below 0^0C. From the above statistics (pre-monsoon and monsoon cases) it may be stated that the

718   mean/median value of CI for the non-spherical particle layer is distributed between 11 and 15, irrespective of environmental

719   humidity and season. BSR values for the non-spherical layer are between 1.4 and 3.5 at 455 nm, whereas little spread in the

720   red channel.

721   **3.4. Illustration of the aerosol-cloud relationship**

722   In this section, an attempt is made to demonstrate the method to identify the relationship, if any, between aerosol

723   and cloud properties observed using balloon observations of the BACIS campaigns. In the present analysis, we have

724   restricted ourselves to only liquid or low-level clouds as aerosol interactions in these cloud categories are well established

725   (Bruce A. Albrecht, 1989; Twomey, 1977).

726   The scheme (discussed in sec. 2) is applied to the 15 balloon soundings of the BACIS campaigns and 6 launches

727   have been observed with low-level cloud and aerosol layers. Further, a scatter plot between logarithm values of the median

728   cloud particle count of the cloud layer and logarithm of median values of aerosol (blue) backscatter below cloud base (for

729   300, 400 and 500m) is plotted in Fig. 132. A linear fit (line) of log-log values is also shown separately for all depths. It is

730 noticed for depths 100 and 200m below the cloud base relationship between aerosol, and the cloud cannot be discussed due

731 to a lack of data points of aerosol backscatter ratio from individual campaigns. This could be the result of the elimination of

732 the high value of COBALD particle backscatter (>3.15) observed in this region (100 and 200m below cloud base). In the

733 cloud boundaries of about 100 and 200m below the cloud base, an intermediate region exists where aerosol transformation to

734 cloud particle/growth takes place. Hence it is tricky to have the aerosol observation in this region. On the other hand, with

735 similar elimination criteria (Section 2), aerosol backscatter could be obtained (from all 5 campaigns) for depths 300m

736 onwards (up to 500m) from the cloud base. A good positive relationship is found between aerosol backscatter and cloud

737 particle count with a statistically significant Pearson correlation coefficient of about 0.9 and slope (ACI index) of 0.77 and

738 0.86 when the aerosol is considered from 300 and 400m below the cloud base, respectively. For a depth of 500m from the

739 cloud base, the slope has decreased to 0.67 (correlation coefficient is also not significant with p-value >0.05) indicating

740 aerosol influence weakens if the region below 400m from the cloud base is considered. Therefore, it may be better to

741 consider aerosols up to a depth of 400m (below the cloud base) for understanding their influence on cloud properties. It is

742 also emphasized that the slope (ACI index) value obtained in this analysis at all depths is well within the theoretical range of

743 0 to 1. However, with a greater number of balloon soundings, it might be possible to have statistically significant aerosol

744 data after constraining similar background/meteorological conditions to delineate their possible effects. Data obtained on 04

745 February 2020 was not considered in the analysis due to the high values of COBALD. The individual uncertainties in BSRb

746 and Nc were assumed to be 5% and the combined uncertainty in the ACI index is estimated as discussed in Sec. 2.4.7

747 (equation.7). It is found that the combined uncertainty in the estimated ACI index is found from 0.01 to 0.23 and 0.08 to

748 0.13, respectively for particle backscatter data from 300 and 400m below cloud base.

749 **4. Summary**

750   The BACIS (Balloon-borne Aerosol Cloud Interaction Studies) field campaigns have been conceptualized and

751 successfully conducted using multiple instruments from Gadanki (13.45^0 N; 79.2^0 E), a location in Southern peninsular India.

752 Meteorological balloon payloads with a combination of lightweight and specialized sondes such as COBALD and CPS have

753 been launched for the first time before a CALIPSO satellite overpass (close by Gadanki). Ground-based Lidars

754 (MPL/Ceilometer/Mie lidar), and Radars (MST Radar/LAWP) were also operated during the campaign period. So far 15

755 balloon soundings have been conducted as part of the BACIS campaigns.

756 During the first two (pilot) campaigns, all essential ground-based and space-borne instruments were made available.

757 Balloon-borne in-situ measurements (CPS and COBALD) are assessed using the data from ground/spaceborne remote

758 sensing instruments (CALIPSO, MPL and a Mie lidar) from two pilot campaigns (early hours of 6 June and 8 July 2017).

759 The comparison shows reasonable agreement within in-situ measurements as well as between ground-based/space-borne and

760 in-situ measurements. It is observed that the in-situ balloon soundings using a combination of specialized (COBALD and

761 CPS) sondes adds to the cloud and aerosol information than can be obtained from an individual ground/spaceborne

762 instrument.

763 To discriminate aerosol from clouds in a profile, combined observations of COBALD and CPS from a campaign

764 held on 27 June 2019 were inferred in detail. Using CPS data, liquid supercooled, and ice clouds were identified. COBALD

765 data of BSR corresponding to the ice clouds was found to be 1-10 (at blue channel) and CI of 10 to 20. In addition to cloud

766 features, CPS has also detected cloud particle layers at low altitudes (under dry conditions). These layers may be regarded as

767 non-spherical (coarse mode) aerosol particle layers as ice clouds (with non-spherical cloud particles) cannot exist at lower

768 heights. An attempt is also made to infer the size of cloud particles using the CPS data of intensity of scattered light (I55)

769 and the COBALD colour index. Based on CPS scattered light, the liquid droplet size (for the above case) is estimated to be

770 2-14 μm, and for ice particles, it is a combination of particles with 80-140 μm and 2-14 μm. The estimates of ice particle

771 sizes using CI data from COBALD supported the size interpretations of ice particles by CPS.

772 Further, combined observations from COBALD and CPS (BSR, CI, and peak particle number concentration data

773 based on information on the cloud phase) are analyzed from multiple (eight) balloon soundings from BACIS Campaigns.

774 From these statistics, it is found that the mean value of CI of ice cloud is found between 18 and 20. BSR (at both

775 wavelengths) have a wide range of values hence threshold values for ice clouds could not be arrived at. However, in some

776 cases, BSR increased with ice clouds of more droplet number concentration. In the case of non-spherical particle (aerosol)

777 layers (in the lower troposphere), the mean values of CI and BSR (at 455 nm) are found to be between 11 to 15 and 1.4 to

778 3.5, respectively. These non-spherical particle layers may correspond to coarse mode (dust) aerosols as discussed.

779   The relationship between aerosol and cloud in low-level (liquid) clouds is illustrated using balloon data from

780   BACIS campaigns. CPS cloud particle count and COBALD particle backscatter at the blue channel were considered as cloud

781   and aerosol proxies, respectively. A scheme is developed to carefully identify the cloud layers from CPS data and particle

782   (aerosol) backscatter below the cloud from COBALD data (in a profile). However, the relationships were analyzed

783   separately using particle backscatter data from 100 to 500m below the base height for the first cloud layer. The results show

784   a statistically significant correlation of 0.9 and a slope (Aerosol-Cloud Interaction index, ACI) of 0.7 (0.86) obtained

785   between particle backscatter from 300m (500m) below the cloud base and the corresponding cloud particle count. The ACI

786   index value obtained is well within the theoretical limits of 0 to 1 indicative of the aerosol activation process of the cloud.

787   The uncertainty in the estimated value of the ACI index is 0.01 to 0.23 and 0.08 to 0.13, respectively for backscatter data

788   from 300 and 400m below the cloud base.

789   Statistical estimates/threshold value of CI, BSR for cloud (liquid/super-cooled/ice) and non-spherical particles

790   attempted here will greatly help to separate a COBALD profile for aerosol and cloud. However, immediate efforts are

791   needed to understand the portion of the COBALD profile with no cloud detection from CPS. This portion of the COBALD

792   profile may correspond to either aerosol with fine mode particles and/or a thin cloud not detectable by a CPS. On the other

793   hand, estimates of size discussed here (from CPS, COBALD) are purely based on Mie theory and laboratory data. However,

794   with assumptions of the log-normal distribution of particles and measurements from COBALD (BSR, CI), the theoretical

795   estimate of the particle size distribution of aerosol/cloud is possible. It makes sense to cross-check rough estimates of size

796   from a CPS with COBALD size distributions rather than using CI variations. It is also planned to add a size distribution

797   measurement to the balloon payload for cross-verification and validation. Apart from this, in some of the cases, we have

798   noticed COBALD return signal saturated for liquid/supercooled cloud in the presence of a thick liquid cloud. Hence the

799   information from a greater number of future launches will help to conclude the statistical figures/threshold values for liquid

800   clouds as well as other cases of clouds, to discriminate the aerosol/cloud in a profile and to better quantify the aerosol-cloud

801   relationship. Further to this, attempts will be made to quantify aerosol-cloud interactions (with the multi-instrument data),

802   particularly the role of vertical wind and turbulence on the aerosol-cloud interactions, and ice cloud interactions, among

803 others. In a nutshell, the results presented in the study indeed demonstrate the potential of the observational
804 approach/method, to understand the aerosol-cloud process.

805 **Code/Data Availability**

806 Data analyzed in the study is made available on Zenodo (10.5281/zenodo.5749293). Data will also be shared
807 with the interested users under the collaboration.

808 **Author Contribution**

809 RKV is responsible for Conceptualization, Conducting experiments, Formal analysis, Visualization, Investigation,
810 Writing-original draft preparation; VRM is responsible for Supervision, helping in Visualization, Writing-review and
811 editing. FM, HR and FGW are responsible for Writing-review and editing; MBL, RRM, and RN helped in Visualization,
812 Writing-review and editing; RN, ARST, HKA, and RBS helped in conducting the experiment, Writing-review and editing;

813 **Competing interest**

814 The authors declare that they have no conflict of interest.

815 **Acknowledgements**

816 The authors would like to thank the Director, NARL for supporting of conducting the field campaigns from NARL, Gadanki.
817 Special thanks to the RADG and ASDG group members of NARL for their cooperation in the operation of Indian MST
818 Radar, LAWP and Mie Lidar, respectively, during the launch period. We also would like to express our thanks to the staff
819 members of ARTG, the balloon launch facility of NARL for extending their kind support for smoothly conducting balloon
820 launches and recovery. The CALIPSO science team is credited for providing the CALIOP data analysed in the study freely
821 available on their webpage (https://www.calipso.larc.nasa.gov). We are also thankful to the Hysplit team for facilitating the
822 running of the HYSPLIT model on their server to simulate the air parcel back trajectories as per the requirement.

823

824 **References**

825 Abbott, T. H. and Cronin, T. W.: Through Increases in Humidity, Science (80-.)., 85(January), 83–85, 2021.

826 Brabec, M., Wienhold, F. G., Wüest, M., Krieger, U. and Peter, T.: A novel radiosonde payload to study upper tropospheric /
827 lower stratospheric aerosol and clouds, 2008.

828 Brabec, M., Wienhold, F. G., Luo, B. P., VÃmel, H., Immler, F., Steiner, P., Hausammann, E., Weers, U. and Peter, T.:
829 Particle backscatter and relative humidity measured across cirrus clouds and comparison with microphysical cirrus
830 modelling, Atmos. Chem. Phys., 12(19), 9135–9148, doi:10.5194/acp-12-9135-2012, 2012.

831 BRUCE A. ALBRECHT: Aerosols, Cloud Microphysics, and Fractional Cloudiness, Science (80-.)., 245(4247), 24–29,

832   1989.

833   Brunamonti, S., Jorge, T., Oelsner, P., Hanumanthu, S., Singh, B. B., Ravi Kumar, K., Sonbawne, S., Meier, S., Singh, D.,

834   Wienhold, F. G., Ping Luo, B., Boettcher, M., Poltera, Y., Jauhiainen, H., Kayastha, R., Karmacharya, J., DIrksen, R., Naja,

835   M., Rex, M., Fadnavis, S. and Peter, T.: Balloon-borne measurements of temperature, water vapor, ozone and aerosol

836   backscatter on the southern slopes of the Himalayas during StratoClim 2016-2017, Atmos. Chem. Phys., 18(21), 15937–

837   15957, doi:10.5194/acp-18-15937-2018, 2018.

838   Brunamonti, S., Martucci, G., Romanens, G., Poltera, Y., Wienhold, F., Haefele, A. and Navas-Guzmán, F.: Validation of

839   aerosol backscatter profiles from Raman lidar and ceilometer using balloon-borne measurements, Atmos. Chem. Phys.

840   Discuss., (May), 1–31, doi:10.5194/acp-2020-294, 2020.

841   Cherian, T., Kumar, Y. B., Reddy, B. S., Optics, G., Limited, A., Nr, R. S. and Road, N.: LIDAR for Atmospheric

842   Measurement and Probing, , 5(84), 5114–5124, 2014.

843   Cirisan, A., Luo, B. P., Engel, I., Wienhold, F. G., Sprenger, M., Krieger, U. K., Weers, U., Romanens, G., Levrat, G.,

844   Jeannet, P., Ruffieux, D., Philipona, R., Calpini, B., Spichtinger, P. and Peter, T.: Balloon-borne match measurements of

845   midlatitude cirrus clouds, Atmos. Chem. Phys., 14(14), 7341–7365, doi:10.5194/acp-14-7341-2014, 2014.

846   COAKLEY, J. A., BERNSTEIN, R. L. and DURKEE, P. A.: Effect of Ship-Stack Effluents on Cloud Reflectivity, Science

847   (80-.)., 237(4818), 1020 LP – 1022, doi:10.1126/science.237.4818.1020, 1987.

848   Corrigan, C. E., Roberts, G. C., Ramana, M. V., Kim, D. and Ramanathan, V.: Capturing vertical profiles of aerosols and

849   black carbon over the Indian Ocean using autonomous unmanned aerial vehicles, Atmos. Chem. Phys., 8(3), 737–747,

850   doi:10.5194/acp-8-737-2008, 2008.

851   Costantino, L. and Bréon, F. M.: Analysis of aerosol-cloud interaction from multi-sensor satellite observations, Geophys.

852   Res. Lett., 37(11), 1–5, doi:10.1029/2009GL041828, 2010.

853   Deshler, T., Hervig, M. E., Hofmann, D. J., Rosen, J. M. and Liley, J. B.: Thirty years of in situ stratospheric aerosol size

854   distribution measurements from Laramie, Wyoming (41°N), using balloon-borne instruments, J. Geophys. Res. Atmos.,

855   108(5), 1–13, doi:10.1029/2002jd002514, 2003.

856   Fan, J., Wang, Y., Rosenfeld, D. and Liu, X.: Review of aerosol-cloud interactions: Mechanisms, significance, and

857   challenges, J. Atmos. Sci., 73(11), 4221–4252, doi:10.1175/JAS-D-16-0037.1, 2016.

858   Fan, J., Rosenfeld, D., Zhang, Y., Giangrande, S. E., Li, Z., Machado, L. A. T., Martin, S. T., Yang, Y., Wang, J., Artaxo, P.,

859   Barbosa, H. M. J., Braga, R. C., Comstock, J. M., Feng, Z., Gao, W., Gomes, H. B., Mei, F., Pöhlker, C., Pöhlker, M. L.,

860   Pöschl, U. and de Souza, R. A. F.: Substantial convection and precipitation enhancements by ultrafine aerosol particles,

861   Science (80-.)., 359(6374), 411–418, doi:10.1126/science.aan8461, 2018.

862   Feingold, G., Eberhard, W. L., Veron, D. E. and Previdi, M.: First measurements of the Twomey indirect effect using

863   ground-based remote sensors, Geophys. Res. Lett., 30(6), 19–22, doi:10.1029/2002GL016633, 2003.

864   Feingold, G., Furrer, R., Pilewskie, P., Remer, L. A., Min, Q. and Jonsson, H.: Aerosol indirect effect studies at Southern

865   Great Plains during the May 2003 Intensive Operations Period, J. Geophys. Res. Atmos., 111(5), 1–13,

doi:10.1029/2004JD005648, 2006.

Fujiwara, M., Shiotani, M., Hasebe, F., Vömel, H., Oltmans, S. J., Ruppert, P. W., Horinouchi, T. and Tsuda, T.: Performance of the Meteolabor "Snow White" chilled-mirror hygrometer in the tropical troposphere: Comparisons with the Vaisala RS80 A/H-Humicap sensors, J. Atmos. Ocean. Technol., 20(11), 1534–1542, doi:10.1175/1520-0426(2003)020<1534:POTMSW>2.0.CO;2, 2003.

~~Fujiwara, M., Sugidachi, T., Arai, T., Shimizu, K., Hayashi, M., Noma, Y., Kawagita, H., Sagara, K., Nakagawa, T., Okumura, S., Inai, Y., Shibata, T. and Iwasaki, S.: Development of a cloud particle sensor for radiosonde sounding, , (May), doi:10.5194/amt-2016-170, 2016a.~~

Fujiwara, M., Sugidachi, T., Arai, T., Shimizu, K., Hayashi, M., Noma, Y., Kawagita, H., Sagara, K., Nakagawa, T., Okumura, S., Inai, Y., Shibata, T., Iwasaki, S. and Shimizu, A.: Development of a cloud particle sensor for radiosonde sounding, Atmos. Meas. Tech., 9(12), 5911–5931, doi:10.5194/amt-9-5911-2016, 2016~~b~~.

Girdwood, J., Smith, H., Stanley, W., Ulanowski, Z., Stopford, C., Chemel, C., Doulgeris, K. M., Brus, D., Campbell, D. and MacKenzie, R.: Design and field campaign validation of a multi-rotor unmanned aerial vehicle and optical particle counter, Atmos. Meas. Tech., 13(12), 6613–6630, doi:10.5194/amt-13-6613-2020, 2020.

Girdwood, J., Stanley, W., Stopford, C. and Brus, D.: Simulation and Field Campaign Evaluation of an Optical Particle Counter on a Fixed-Wing UAV, Atmos. Meas. Tech. Discuss., (October), 1–26, 2021.

Grosvenor, D. P., Sourdeval, O., Zuidema, P., Ackerman, A., Alexandrov, M. D., Bennartz, R., Boers, R., Cairns, B., Chiu, J. C., Christensen, M., Deneke, H., Diamond, M., Feingold, G., Fridlind, A., Hünerbein, A., Knist, C., Kollias, P., Marshak, A., McCoy, D., Merk, D., Painemal, D., Rausch, J., Rosenfeld, D., Russchenberg, H., Seifert, P., Sinclair, K., Stier, P., van Diedenhoven, B., Wendisch, M., Werner, F., Wood, R., Zhang, Z. and Quaas, J.: Remote Sensing of Droplet Number Concentration in Warm Clouds: A Review of the Current State of Knowledge and Perspectives, Rev. Geophys., 56(2), 409–453, doi:10.1029/2017RG000593, 2018.

Gupta, G., Ratnam, M. V., Madhavan, B. L., Prasad, P. and Narayanamurthy, C. S.: Vertical and spatial distribution of elevated aerosol layers obtained using long-term ground-based and space-borne lidar observations, Atmos. Environ., 246(December 2020), 118172, doi:10.1016/j.atmosenv.2020.118172, 2021.

Hanumanthu, S., Vogel, B., Müller, R., Brunamonti, S., Fadnavis, S., Li, D., Ölsner, P., Naja, M., Singh, B. B., Kumar, K. R., Sonbawne, S., Jauhiainen, H., Vömel, H., Luo, B., Jorge, T., Wienhold, F. G., Dirkson, R. and Peter, T.: Strong day-to-day variability of the Asian Tropopause Aerosol Layer (ATAL) in August 2016 at the Himalayan foothills, Atmos. Chem. Phys., 20(22), 14273–14302, doi:10.5194/acp-20-14273-2020, 2020.

Haywood, J. and Boucher, O.: Estimates of the direct and indirect radiative forcing due to tropospheric aerosols: A review, Rev. Geophys., 38(4), 513–543, doi:10.1029/1999RG000078, 2000.

Inoue, J., Sato, K., Tobo, Y., Taketani, F. and Maturilli, M.: Advanced method for estimating the number concentration of cloud water and liquid water content observed by cloud particle sensor sondes, Atmos. Meas. Tech. Discuss., 1–35, doi:10.5194/amt-2020-476, 2021.

900 IPCC: Climate Change 2021: The Physical Science Basis. Contribution of Working Group I to the Sixth Assessment Report

901 of the Intergovernmental Panel on Climate Change, edited by V. Masson-Delmotte, P. Zhai, A. Pirani, S. L. Connors, C.

902 Péan, S. Berger, N. Caud, Y. Chen, L. Goldfarb, M. I. Gomis, M. Huang, K. Leitzell, E. Lonnoy, J. B. R. Matthews, T. K.

903 Maycock, T. Waterfield, O. Yelekçi, R. Yu, and B. Zhou, Cambridge University Press, Cambridge, United Kingdom and

904 New York, NY, USA., 2021.

905 Jain, C. D., Madhavan, B. L. and Ratnam, M. V.: Source apportionment of rainwater chemical composition to investigate the

906 transport of lower atmospheric pollutants to the UTLS region, Environ. Pollut., 248, 166–174,

907 doi:10.1016/j.envpol.2019.02.007, 2019.

908 Jose, S., Nair, V. S. and Babu, S. S.: Anthropogenic emissions from South Asia reverses the aerosol indirect effect over the

909 northern Indian Ocean, Sci. Rep., 10(1), 1–8, doi:10.1038/s41598-020-74897-x, 2020.

910 Kezoudi, M., Tesche, M., Smith, H., Tsekeri, A., Baars, H., Dollner, M., Estelleácute;s, V., Bü¨hl, J., Weinzierl, B.,

911 Ulanowski, Z., Mü¨ller, D. and Amiridis, V.: Measurement report: Balloon-borne in situ profiling of Saharan dust over

912 Cyprus with the UCASS optical particle counter, Atmos. Chem. Phys., 21(9), 6781–6797, doi:10.5194/acp-21-6781-2021,

913 2021.

914 Kobayashi, E., Hoshino, S., Iwabuchi, M., Sugidachi, T., Shimizu, K. and Fujiwara, M.: Comparison of the GRUAN data

915 products for Meisei RS-11G and Vaisala RS92-SGP radiosondes at Tateno (36.06°N, 140.13°E), Japan, Atmos. Meas. Tech.,

916 12(6), 3039–3065, doi:10.5194/amt-12-3039-2019, 2019.

917 Koren, I., Remer, L. A., Altaratz, O., Martins, J. V. and Davidi, A.: Aerosol-induced changes of convective cloud anvils

918 produce strong climate warming, Atmos. Chem. Phys., 10(10), 5001–5010, doi:10.5194/acp-10-5001-2010, 2010.

919 Kulkarni, J. R., Maheskumar, R. S., Morwal, S. B., Padma Kumari, B., Konwar, M., Deshpande, C. G., Joshi, R. R.,

920 Bhalwankar, R. V., Pandithurai, G., Safai, P. D., Narkhedkar, S. G., Dani, K. K., Nath, A., Nair, S., Sapre, V. V., Puranik, P.

921 V., Kandalgaonkar, S. S., Mujumdar, V. R., Khaladkar, R. M., Vijayakumar, R., Prabha, T. V. and Goswami, B. N.: The

922 cloud aerosol interaction and precipitation enhancement experiment (CAIPEEX): Overview and preliminary results, Curr.

923 Sci., 102(3), 413–425, 2012.

924 L'Ecuyer, T. S.: Touring the atmosphere aboard the A-Train (vol 63, pg 36, 2010), Phys. Today, 64(8), 10, 2011.

925 Lohmann, U.: Aerosol effects on clouds and climate, Space Sci. Rev., 125(1–4), 129–137, doi:10.1007/s11214-006-9051-8,

926 2006.

927 Lohmann, U. and Feichter, J.: Global indirect aerosol effects: a review, Atmos. Chem. Phys. Discuss., 4(6), 7561–7614,

928 doi:10.5194/acpd-4-7561-2004, 2004.

929 Mamali, D., Marinou, E., Sciare, J., Pikridas, M., Kokkalis, P., Kottas, M., Binietoglou, I., Tsekeri, A., Keleshis, C.,

930 Engelmann, R., Baars, H., Ansmann, A., Amiridis, V., Russchenberg, H. and Biskos, G.: Vertical profiles of aerosol mass

931 concentration derived by unmanned airborne in situ and remote sensing instruments during dust events, Atmos. Meas. Tech.,

932 11(5), 2897–2910, doi:10.5194/amt-11-2897-2018, 2018.

933 McComiskey, A. and Feingold, G.: The scale problem in quantifying aerosol indirect effects, Atmos. Chem. Phys., 12(2),

934 1031–1049, doi:10.5194/acp-12-1031-2012, 2012.

935 McComiskey, A., Feingold, G., Frisch, A. S., Turner, D. D., Miller, M. A., Chiu, J. C., Min, Q. and Ogren, J. A.: An

936 assessment of aerosol-cloud interactions in marine stratus clouds based on surface remote sensing, J. Geophys. Res. Atmos.,

937 114(9), 1–15, doi:10.1029/2008JD011006, 2009.

938 Mishra, M. K., Rajeev, K., Thampi, B. V., Parameswaran, K. and Nair, A. K. M.: Micro pulse lidar observations of mineral

939 dust layer in the lower troposphere over the southwest coast of Peninsular India during the Asian summer monsoon season,

940 J. Atmos. Solar-Terrestrial Phys., 72(17), 1251–1259, doi:10.1016/j.jastp.2010.08.012, 2010.

941 Murphy, D. M. and Koop, T.: Review of the vapour pressures of ice and supercooled water for atmospheric applications, Q.

942 J. R. Meteorol. Soc., 131(608), 1539–1565, doi:10.1256/qj.04.94, 2005.

943 Narendra Reddy, N., Venkat Ratnam, M., Basha, G. and Ravikiran, V.: Cloud vertical structure over a tropical station

944 obtained using long-term high resolution Radiosonde measurements, Atmos. Chem. Phys. Discuss., 1–49, doi:10.5194/acp-

945 2018-194, 2018.

946 Pandit, A. K., Gadhavi, H., Ratnam, M. V., Jayaraman, A., Raghunath, K. and Rao, S. V. B.: Characteristics of cirrus clouds

947 and tropical tropopause layer: Seasonal variation and long-term trends, J. Atmos. Solar-Terrestrial Phys., 121(PB), 248–256,

948 doi:10.1016/j.jastp.2014.07.008, 2014.

949 Pandit, A. K., Gadhavi, H. S., Ratnam, M. V., Raghunath, K., Rao, S. V. B. and Jayaraman, A.: Long-term trend analysis

950 and climatology of tropical cirrus clouds using 16 years of lidar data set over Southern India, Atmos. Chem. Phys., 15(24),

951 13833–13848, doi:10.5194/acp-15-13833-2015, 2015.

952 Pandithurai, G., Takamura, T., Yamaguchi, J., Miyagi, K., Takano, T., Ishizaka, Y., Dipu, S. and Shimizu, A.: Aerosol effect

953 on cloud droplet size as monitored from surface-based remote sensing over East China Sea region, Geophys. Res. Lett.,

954 36(13), 1–5, doi:10.1029/2009GL038451, 2009.

955 Prasad, P., Raman, M. R., Ratnam, M. V., Ravikiran, V., Madhavan, B. L. and Bhaskara, S. V.: Nocturnal, seasonal and

956 intra-annual variability of tropospheric aerosols observed using ground-based and space-borne lidars over a tropical location

957 of India, Atmos. Environ., 213(May), 185–198, doi:10.1016/j.atmosenv.2019.06.008, 2019.

958 Radke, L. F., Coakley, J. A. and King, M. D.: Direct and remote sensing observations of the effects of ships on clouds,

959 Science (80-.)., 246(4934), 1146–1149, doi:10.1126/science.246.4934.1146, 1989.

960 Rao, P. B., Jain, A. R., Kishore, P., Balamuralidhar, P., Damle, S. H. and Viswanathan, G.: Indian MST radar 1. System

961 description and sample vector wind measurements in ST mode, Radio Sci., 30(4), 1125–1138, doi:10.1029/95RS00787,

962 1995.

963 Ratnam, M. V., Prasad, P., Raman, M. R., Ravikiran, V., Bhaskara, S. V., Murthy, B. V. K. and Jayaraman, A.: Role of

964 dynamics on the formation and maintenance of the elevated aerosol layer during monsoon season over south-east peninsular

965 India, , 188(June), 43–49, doi:10.1016/j.atmosenv.2018.06.023, 2018.

966 Redemann, J., Wood, R., Zuidema, P., Doherty, S., Luna, B., LeBlanc, S., Diamond, M., Shinozuka, Y., Chang, I., Ueyama,

967 R., Pfister, L., Ryoo, J., Dobracki, A., da Silva, A., Longo, K., Kacenelenbogen, M., Flynn, C., Pistone, K., Knox, N., Piketh,

968 S., Haywood, J., Formenti, P., Mallet, M., Stier, P., Ackerman, A., Bauer, S., Fridlind, A., Carmichael, G., Saide, P.,

969 Ferrada, G., Howell, S., Freitag, S., Cairns, B., Holben, B., Knobelspiesse, K., Tanelli, S., L'Ecuyer, T., Dzambo, A., Sy, O.,

970 McFarquhar, G., Poellot, M., Gupta, S., O'Brien, J., Nenes, A., Kacarab, M., Wong, J., Small-Griswold, J., Thornhill, K.,

971 Noone, D., Podolske, J., Schmidt, K. S., Pilewskie, P., Chen, H., Cochrane, S., Sedlacek, A., Lang, T., Stith, E., Segal-

972 Rozenhaimer, M., Ferrare, R., Burton, S., Hostetler, C., Diner, D., Platnick, S., Myers, J., Meyer, K., Spangenberg, D.,

973 Maring, H. and Gao, L.: An overview of the ORACLES (ObseRvations of Aerosols above CLouds and their intEractionS)

974 project: aerosol-cloud-radiation interactions in the Southeast Atlantic basin, Atmos. Chem. Phys., 1–82, doi:10.5194/acp-

975 2020-449, 2020.

976 Rosen, J. M. and Kjome, N. T.: Backscattersonde: a new instrument for atmospheric aerosol research, Appl. Opt., 30(12),

977 1552, doi:10.1364/ao.30.001552, 1991.

978 Rosenfeld, D., Lohmann, U., Raga, G. B., O'Dowd, C. D., Kulmala, M., Fuzzi, S., Reissell, A. and Andreae, M. O.: Flood or

979 drought: How do aerosols affect precipitation?, Science (80-.)., 321(5894), 1309–1313, doi:10.1126/science.1160606, 2008.

980 Rosenfeld, D., Sherwood, S., Wood, R. and Donner, L.: Climate Effects of Aerosol-Cloud Interactions, Science (80-.).,

981 343(6169), 379 LP – 380, doi:10.1126/science.1247490, 2014a.

982 Rosenfeld, D., Andreae, M. O., Asmi, A., Chin, M., Leeuw, G., Donovan, D. P., Kahn, R., Kinne, S., Kivekäs, N., Kulmala,

983 M., Lau, W., Schmidt, K. S., Suni, T., Wagner, T., Wild, M. and Quaas, J.: Reviews of Geophysics, , 1–59,

984 doi:10.1002/2013RG000441.Received, 2014b.

985 Sarna, K. and Russchenberg, H. W. J.: Ground-based remote sensing scheme for monitoring aerosol-cloud interactions,

986 Atmos. Meas. Tech., 9(3), 1039–1050, doi:10.5194/amt-9-1039-2016, 2016.

987 Sarna, K. and Russchenberg, H. W. J.: Monitoring aerosol-cloud interactions at the CESAR Observatory in the Netherlands,

988 Atmos. Meas. Tech., 10(5), 1987–1997, doi:10.5194/amt-10-1987-2017, 2017.

989 Sathiyamoorthy, V., Mahesh, C., Gopalan, K., Prakash, S., Shukla, B. P. and Mathur, A. K.: Characteristics of low clouds

990 over the Arabian Sea, , 118(December), 489–503, doi:10.1002/2013JD020553, 2013.

991 Schmidt, J., Ansmann, A., Bühl, J., Baars, H., Wandinger, U., Müller, D. and Malinka, A. V.: Dual-FOV raman and Doppler

992 lidar studies of aerosol-cloud interactions: Simultaneous profiling of aerosols, warm-cloud properties, and vertical wind, J.

993 Geophys. Res., 119(9), 5512–5527, doi:10.1002/2013JD020424, 2014.

994 Schmidt, J., Ansmann, A., Bühl, J. and Wandinger, U.: Strong aerosol-cloud interaction in altocumulus during updraft

995 periods: Lidar observations over central Europe, Atmos. Chem. Phys., 15(18), 10687–10700, doi:10.5194/acp-15-10687-

996 2015, 2015.

997 Seinfeld, J. H., Bretherton, C., Carslaw, K. S., Coe, H., DeMott, P. J., Dunlea, E. J., Feingold, G., Ghan, S., Guenther, A. B.,

998 Kahn, R., Kraucunas, I., Kreidenweis, S. M., Molina, M. J., Nenes, A., Penner, J. E., Prather, K. A., Ramanathan, V.,

999 Ramaswamy, V., Rasch, P. J., Ravishankara, A. R., Rosenfeld, D., Stephens, G. and Wood, R.: Improving our fundamental

1000 understanding of the role of aerosol-cloud interactions in the climate system, Proc. Natl. Acad. Sci. U. S. A., 113(21), 5781–

1001 5790, doi:10.1073/pnas.1514043113, 2016.

Sena, E. T., McComiskey, A. and Feingold, G.: A long-term study of aerosol-cloud interactions and their radiative effect at the Southern Great Plains using ground-based measurements, Atmos. Chem. Phys., 16(17), 11301–11318, doi:10.5194/acp-16-11301-2016, 2016.

Small, J. D., Chuang, P. Y., Feingold, G. and Jiang, H.: Can aerosol decrease cloud lifetime?, Geophys. Res. Lett., 36(16), 1–5, doi:10.1029/2009GL038888, 2009.

Smith, H. R., Ulanowski, Z., Kaye, P. H., Hirst, E., Stanley, W., Kaye, R., Wieser, A., Stopford, C., Kezoudi, M., Girdwood, J., Greenaway, R. and Mackenzie, R.: The Universal Cloud and Aerosol Sounding System (UCASS): A low-cost miniature optical particle counter for use in dropsonde or balloon-borne sounding systems, Atmos. Meas. Tech., 12(12), 6579–6599, doi:10.5194/amt-12-6579-2019, 2019.

Srinivasulu, P., Yasodha, P., Kamaraj, P., Rao, T. N., Jayaraman, A., Reddy, S. N. and Satyanarayana, S.: 1280-MHz active array radar wind profiler for lower atmosphere: System description and data validation, J. Atmos. Ocean. Technol., 29(10), 1455–1470, doi:10.1175/JTECH-D-12-00030.1, 2012.

Stein, A. F., Draxler, R. R., Rolph, G. D., Stunder, B. J. B., Cohen, M. D. and Ngan, F.: Noaa's hysplit atmospheric transport and dispersion modeling system, Bull. Am. Meteorol. Soc., 96(12), 2059–2077, doi:10.1175/BAMS-D-14-00110.1, 2015.

Twomey, S.: The Influence of Pollution on the Shortwave Albedo of Clouds, J. Atmos. Sci., 34(7), 1149–1152, doi:10.1175/1520-0469(1977)034<1149:TIOPOT>2.0.CO;2, 1977.

Vernier, J., Fairlie, T. D., Natarajan, M., Wienhold, F. G., Bian, J., Martinsson, B. G., Crumeyrolle, S., Thomason, L. W. and Bedka, K. M.: Journal of Geophysical Research : Atmospheres, , doi:10.1002/2014JD022372.Received, 2015.

Vernier, J. P., Fairlie, T. D., Deshler, T., Venkat Ratnam, M., Gadhavi, H., Kumar, B. S., Natarajan, M., Pandit, A. K., Akhil Raj, S. T., Hemanth Kumar, A., Jayaraman, A., Singh, A. K., Rastogi, N., Sinha, P. R., Kumar, S., Tiwari, S., Wegner, T., Baker, N., Vignelles, D., Stenchikov, G., Shevchenko, I., Smith, J., Bedka, K., Kesarkar, A., Singh, V., Bhate, J., Ravikiran, V., Durga Rao, M., Ravindrababu, S., Patel, A., Vernier, H., Wienhold, F. G., Liu, H., Knepp, T. N., Thomason, L., Crawford, J., Ziemba, L., Moore, J., Crumeyrolle, S., Williamson, M., Berthet, G., Jégou, F. and Renard, J. B.: BATAL: The balloon measurement campaigns of the Asian tropopause aerosol layer, Bull. Am. Meteorol. Soc., 99(5), 955–973, doi:10.1175/BAMS-D-17-0014.1, 2018.

Vernier, J. P., Kalnajs, L., Diaz, J. A., Reese, T., Corrales, E., Alan, A., Vernier, H., Holland, L., Patel, A., Rastogi, N., Wienhold, F., Carn, S., Krotkov, N. and Murray, J.: VolKilau: Volcano rapid response balloon campaign during the 2018 Kilauea eruption, Bull. Am. Meteorol. Soc., 101(10), E1602–E1618, doi:10.1175/BAMS-D-19-0011.1, 2020.

Weinzierl, B., Ansmann, A., Prospero, J. M., Althausen, D., Benker, N., Chouza, F., Dollner, M., Farrell, D., Fomba, W. K., Freudenthaler, V., Gasteiger, J., Groß, S., Haarig, M., Heinold, B., Kandler, K., Kristensen, T. B., Mayol-Bracero, O. L., Müller, T., Reitebuch, O., Sauer, D., Schäfler, A., Schepanski, K., Spanu, A., Tegen, I., Toledano, C. and Walser, A.: The Saharan aerosol long-range transport and aerosol-cloud-interaction experiment: Overview and selected highlights, Bull. Am. Meteorol. Soc., 98(7), 1427–1451, doi:10.1175/BAMS-D-15-00142.1, 2017.

Wiegner, M., Madonna, F., Binietoglou, I., Forkel, R., Gasteiger, J., Geiß, A., Pappalardo, G., Schäfer, K. and Thomas, W.:

1036 What is the benefit of ceilometers for aerosol remote sensing? An answer from EARLINET, Atmos. Meas. Tech., 7(7),

1037 1979–1997, doi:10.5194/amt-7-1979-2014, 2014.

1038 Winker, D. M., Hunt, W. H. and McGill, M. J.: Initial performance assessment of CALIOP, Geophys. Res. Lett., 34(19), 1–

1039 5, doi:10.1029/2007GL030135, 2007.

1040

1041

1042 **Tables**

1043

1044 **Table 1.** List of instruments deployed (in BACIS) and the corresponding physical parameters obtained.

1045

Sl. No.	Instrument	Purpose	Physical quantity (Unit)
1	CALIPSO	Aerosol and cloud profiling	Total attenuated backscatter($km^{-1} sr^{-1}$)
2	MPL	Aerosol and cloud profiling	Backscatter coefficient($m^{-1}sr^{-1}$)
3	Mie Lidar	Aerosol and cloud profiling	Backscatter coefficient($km^{-1}sr^{-1}$)
4	COBALD	In-situ measurement of aerosol and cloud particles	Backscatter ratio
5	CPS	In situ measurement of cloud particles	Cloud particle number concentration(#/cc), degree of polarization(DOP)
6	MST Radar	3-D Wind components, turbulence	Horizontal and vertical wind components(m/s)
7	LAWP	3-D Wind components, turbulence	Horizontal and vertical wind components (m/s)
8	MWR	Meteorological parameters and cloud	Temperature(^{0}C), RH(%) and cloud liquid water content(g/m^3)
9	ICON	Ambient aerosol	BC concentration ($\mu g/m^3$), Scattering coefficient and absorption coefficient (m^{-1})
10	Ceilometer	Boundary layer, cloud and aerosol	Backscatter coefficient($km^{-1}sr^{-1}$)

1046
1047
1048
1049
1050
1051
1052
1053
1054
1055
1056
1057
1058
1059
1060
1061

1062   **Table. 2.** Date and time of the BACIS campaigns and the instruments operated during the corresponding campaigns.

1063

S. No.	Date & Time (LT)	MPL	Mie	Ceil	CPS	COB	MST	MWR	Aeth	CALI	LAWP
1	06-06-2017; 01:57	Y	Y	N	Y	Y	Y	N	Y	Y	Y
2	08-07-2017; 01:36	Y	Y	N	Y	Y	N	N	Y	Y	Y
3	29-09-2018; 01:46	Y	Y	N	Y	Y	N	N	Y	N	Y
4	01-11-2018; 22:13	N	Y	N	Y	Y	N	N	Y	N	Y
5	23-03-2019; 02:36	N	Y	Y	Y	Y	Y	N	Y	N	Y
6	30-04-2019; 23:16	N	Y	Y	Y	Y	Y	N	Y	N	Y
7	30-05-2019; 23:46	N	Y	Y	Y	Y	Y	N	Y	N	Y
8	27-06-2019; 23:45	N	Y	Y	Y	Y	Y	N	Y	N	Y
9	28-08-2019; 23:42	N	Y	Y	Y	Y	Y	N	Y	N	Y
10	09-10-2019; 23:36	N	Y	Y	Y	Y	Y	N	Y	N	Y
11	20-12-2019; 21:20	N	Y	Y	Y	Y	Y	Y	Y	N	Y
12	04-02-2020; 00:27	N	Y	Y	Y	Y	Y	N	Y	N	Y
13	10-03-2020; 00:26	N	Y	Y	Y	Y	Y	N	Y	N	Y
14	19-06-2020; 23:26	N	Y	Y	Y	Y	Y	Y	Y	N	Y
15	19-08-2020; 22:39	N	Y	Y	Y	Y	Y	N	Y	N	Y

MPL – Micro Pulse Lidar; Mie – Mie Lidar; Ceil – Ceilometer; CPS – Cloud Particle Sensor (CPS);

COB – Compact Optical Backscatter AerosoL Detector (COBALD); MST – Indian MST Radar; LAWP – Lower

Atmospheric Wind Profiler (LAWP); Aeth – Aethalometer; CALI – Calipso; MWR – Micro Wave Radiometer.

1064

1065

Table 3. Colour Index (CI) and other physical parameters of the ice clouds. The backscatter ratio (BSR) in normal (Italic)
font is for a 450 nm (940 nm) channel.

1066
1067
1068

Date	Campaign no	Ice cloud altitude (km)	Temperature range (^{0}C)	RH condition	Mean (median) CI	Mean (median) BSR	Range of peak ice particle no conc. (#/cc)
06-Jun-2017	1	13- 15.5	-53 to -74	~ SRH	19.2 (19.2)	5.6(4.8) *90.4(73)*	10^{-2} to 10^{-1}
08-Jul-2017	2	10.5-16	-34 to -78	> SRH	18.7(18.6)	3(2.9) *37.5(35.2)*	10^{-2} to 10^{-1}
01-Nov-2018	4	12-12.6	-47 to -53	> SRH	19.5	17.2(17.5) *318(313.5)*	10^{-1} to 1
30-Apr-2019	6	9.3-16	-22 to -79	~SRH	19.4(19.3)	16.4(8.6) *302(147)*	10^{-1} to 1
30-May-2019	7	16.2-17.4	-78 to -84.5	<SRH	18	1.6(1.4) *12.2(8.7)*	10^{-3} to 10^{-2}
27-Jun-2019	8	9.4-10.7	-23.7 to -35.2	>SRH	19.3(17.9)	5.1(3.1) *74.8(43.2)*	10^{-1} to 1
19-Jun-2020	14	14.2-15.4	-62 to -75	<SRH	21	7.9(7.9) *147.4(143.2)*	10^{-1} to 1

1069
1070

1071

1072 **Table 4.** Colour Index (CI) and backscatter ratio (BSR) of non-spherical (coarse) particle layers as identified by
1073 CPS

1074 sonde. The BSR in the normal (italic) font is 450 nm (940 nm). Blue (red) colour values are observed in the
1075 monsoon (pre-monsoon) months.
1076

Campaign Date	Non-spherical layer altitude (km)	Temperature range (^{0}C)	RH range (%)	Mean (median) CI	Mean (median) BSR
06-Jun-2017	0.5-2.5	27.6 to 15.5	63.5-81.3	12.3(12.5)	1.45(1.4) *6.5(6)*
08-Jul-2017	0.5-2.5	25.3 to 14.7	64.2-96.4	14.6(14.8)	2 *15.8*
29-Sep-2018	0.5-1	22.6 to 20	92-94	12.3	3.3(3.2) *30(29)*
27-Jun-2019	0.5-1.5	27.6 to 19.8	57.3-70.3	11.4	1.6 *7.6*
19-Jun-2020	0.5-2.5	28.8 to 14.2	57.2-94.4	12.6(12.8)	1.6 *8(8.1)*
23-Mar-2019	1.5-3.5	23 to 6.5	32.7-70.3	12.6(12.8)	2 *13*
30-Apr-2019	0.5-4	28 to 4.5	60.2-97.3	12.2(12.6)	3.3(2.6) *28(21.5)*
30-May-2019	0.5-5	28.8 to -0.1	60-98	11.7(11.6)	3.2(2.9) *25.7(22)*

1077
1078

1079
1080
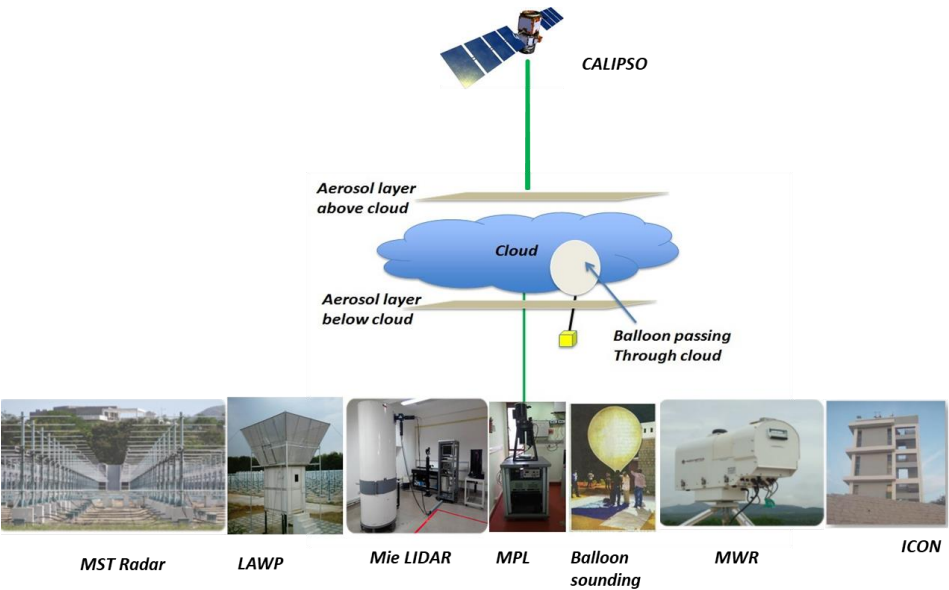
1081
1082 **Figure 1.** Schematic diagram showing the observational concept of the Balloon-borne Aerosol Cloud Interaction Studies
1083   (BACIS) campaign.
1084
1085
1086
1087
1088
1089
1090
1091
1092
1093
1094
1095
1096
1097
1098
1099
1100
1101
1102
1103
1104
1105
1106
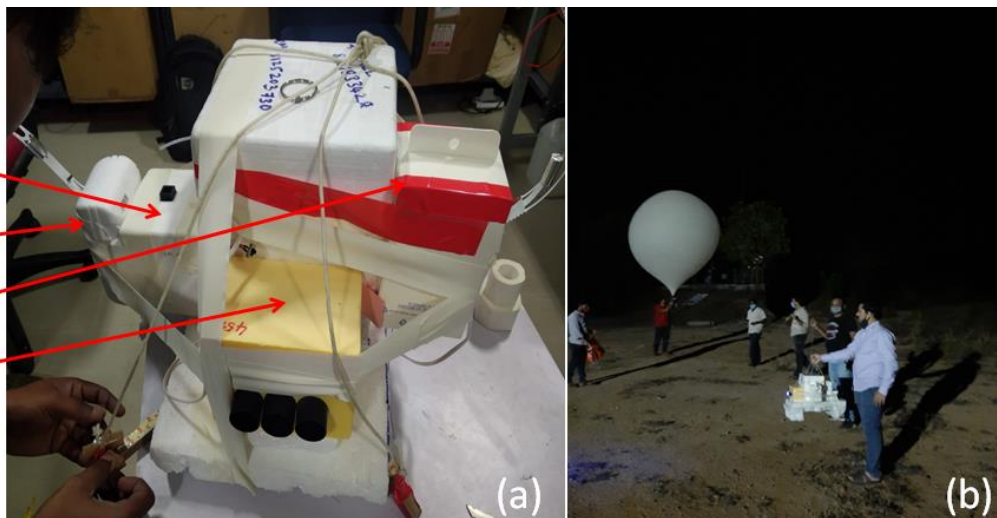
Figure 2. Photograph shows (a) the balloon payload with COBALD, iMet radiosonde, CPS, RS-11G radiosonde, and (b) pre-launch preparations at the launch field with the payload and balloon.

1117
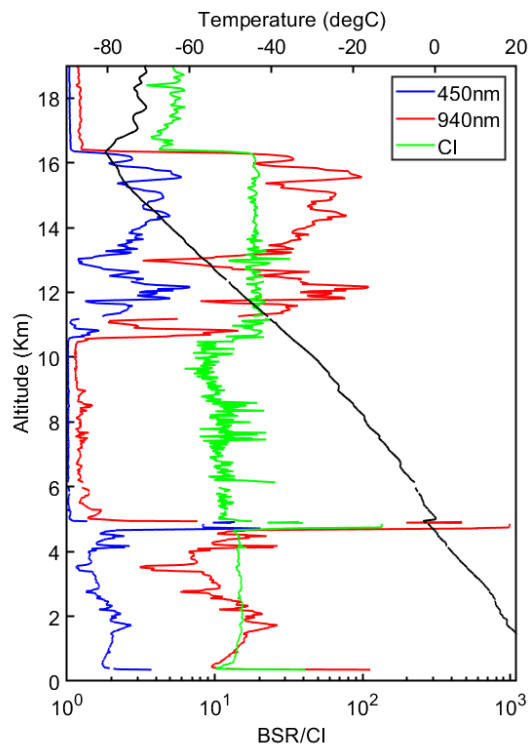
Figure 3. Backscatter ratio (BSR) at blue (450 nm) and red (940 nm) channels were obtained using a COBALD sonde launched during the second pilot campaign (08 July 2017). Colour Index (CI) estimated from BSR at both channels is also shown (in green colour).

1121

1122

1123

1124

1125

1126

1127

1128

1129

1130

1131
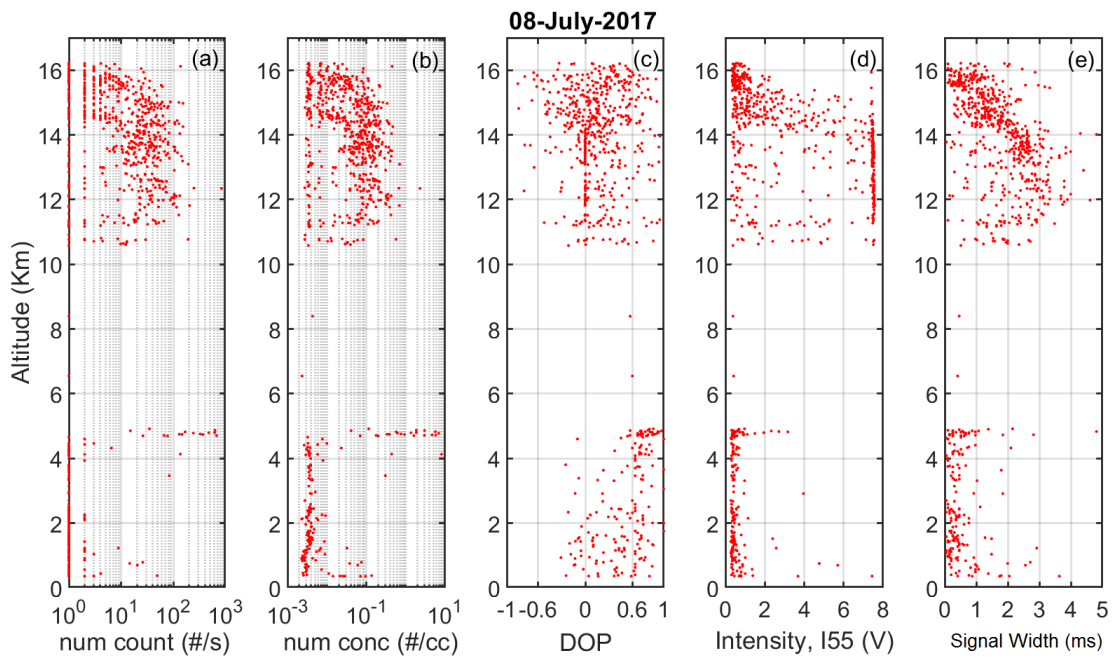
Figure 4. CPS measurements collected from the second pilot campaign (08 July 2017) showing (a) cloud particle number count (corrected), #/s (b) cloud particle number concentration, #/cm^3 (c) Degree of polarization of a cloud particle, DOP (d) the intensity of light scattered at 55 degrees angle in Volts and (e) the particle signal width in ms.

1147

1148
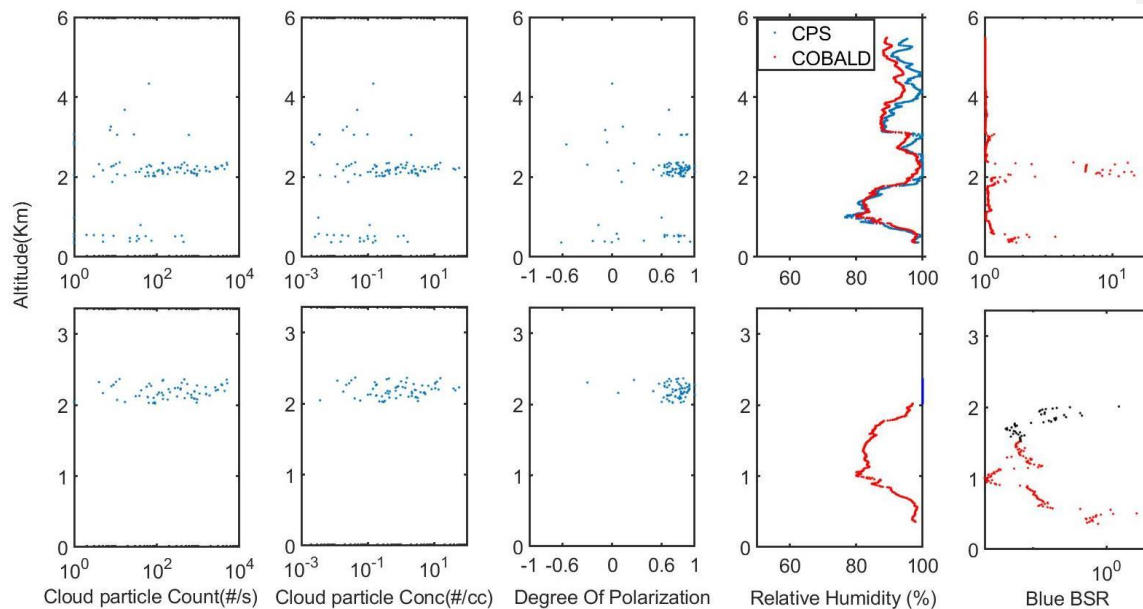
1149 **Figure 5**. The top panel shows COBALD and CPS observations from a sounding held on 01 November 2018 up to the

1150   altitude of 6 km (as the focus is on the liquid cloud region). The bottom panel shows the same parameters but for the

1151   portion of the same profile where liquid cloud (blue dots) and aerosol (from cloud base to 500 m below) were identified by

1152   the scheme.

1153

1154

1155

1156

1157
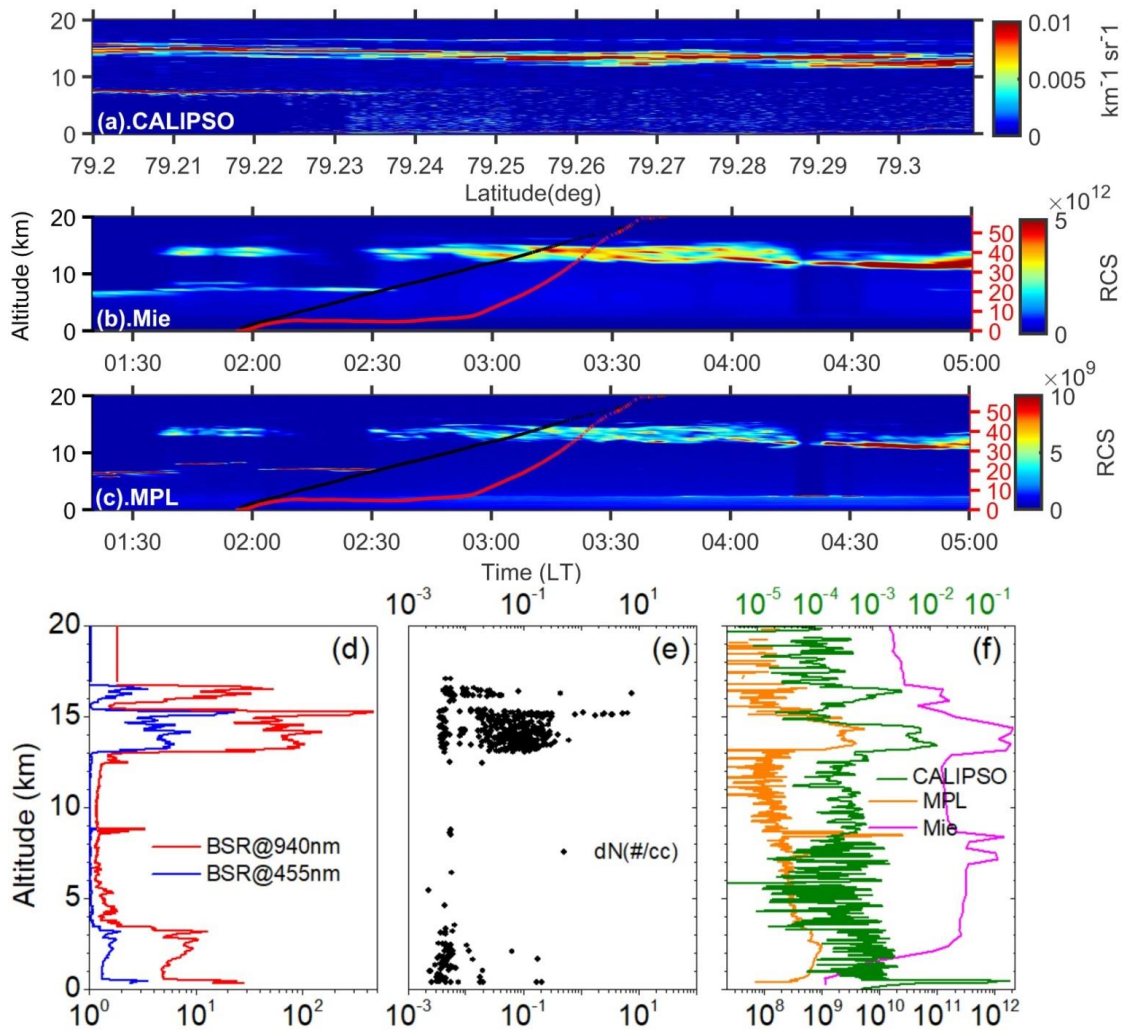
Figure 6. Multi-instrument data from a balloon sounding held in the early hours of 06 June 2017. The total attenuated backscatter from (a) CALIPSO and temporal variation in range corrected signal from (b) Mie lidar and (c) MPL. The red (black) lines overplotted on contour maps (b) and (c) represent balloon drift (altitude) in km with time. Drift as a function of time can be read with the right y-axis (red font) and altitude as a function of time can be read with the left y-axis. The profiles of BSR at two channels from COBALD (blue and red-coloured lines), particle number concentration from CPS (black coloured dots), RCS from MPL (orange), Mie lidar (magenta) and total attenuated backscatter from CALIPSO (olive green) lines shown in (d), (e) and (f) respectively.
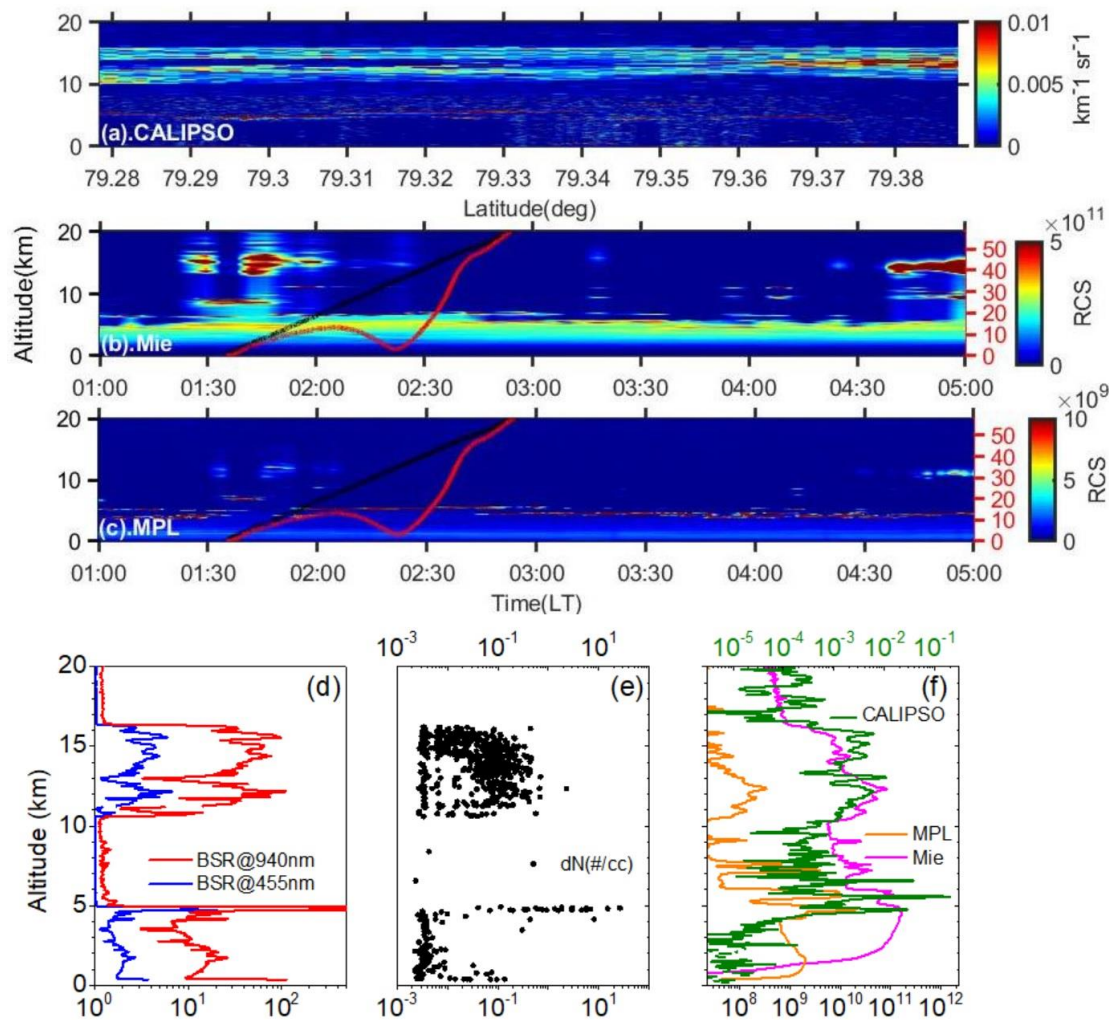
Figure 7. Same as Figure 6 but for the case of the second pilot campaign (08 July 2017).

1173
1174
1175 Figure.8: Google map of the balloon launch facility, remote sensing apparatus at NARL.

Formatted: Font:

Formatted: Normal, Indent: First li
0 cm

1176
1177

1178

1179

1180
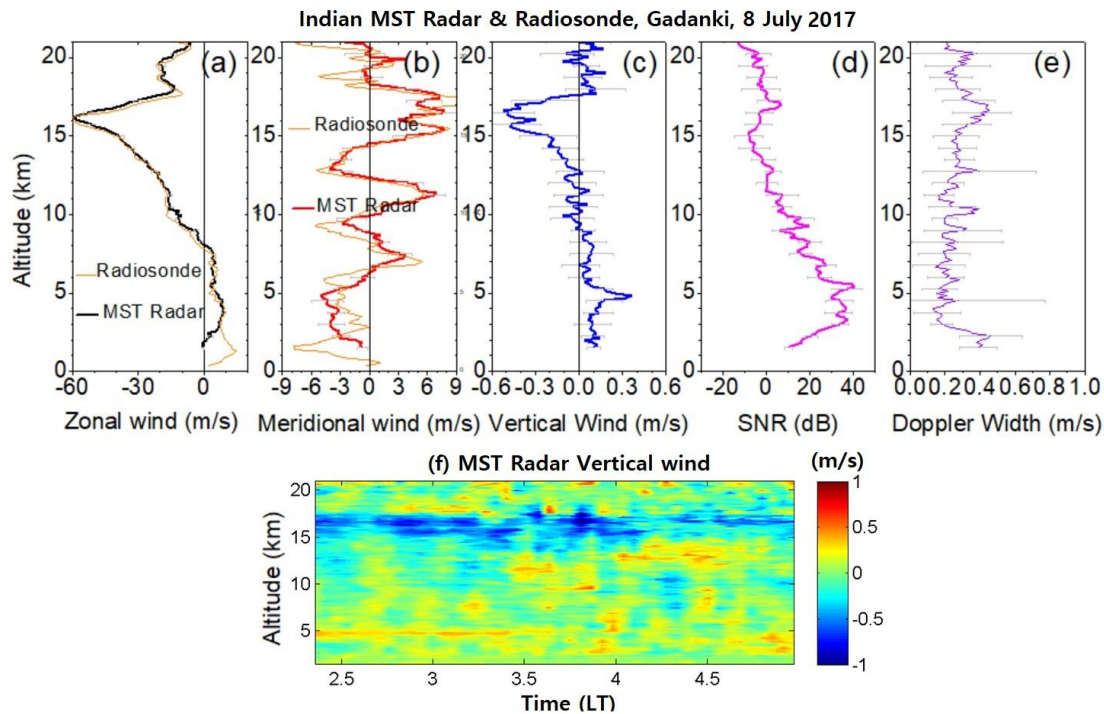
1181 **Figure 89**. Profiles of (a) zonal wind, (b) meridional wind, (c) Vertical wind, (d) Signal to Noise Ratio (SNR) and (e)
1182 Doppler Width were obtained from Indian MST radar on 8 July 2017 averaged during 02:30 LT to 03:30 LT. Horizontal
1183 bars show standard deviation. Radiosonde observed zonal and meridional winds are also superimposed in the respective
1184 panels. (f) Time-altitude section of vertical wind obtained from Indian MST radar during the radiosonde launch time.
1185
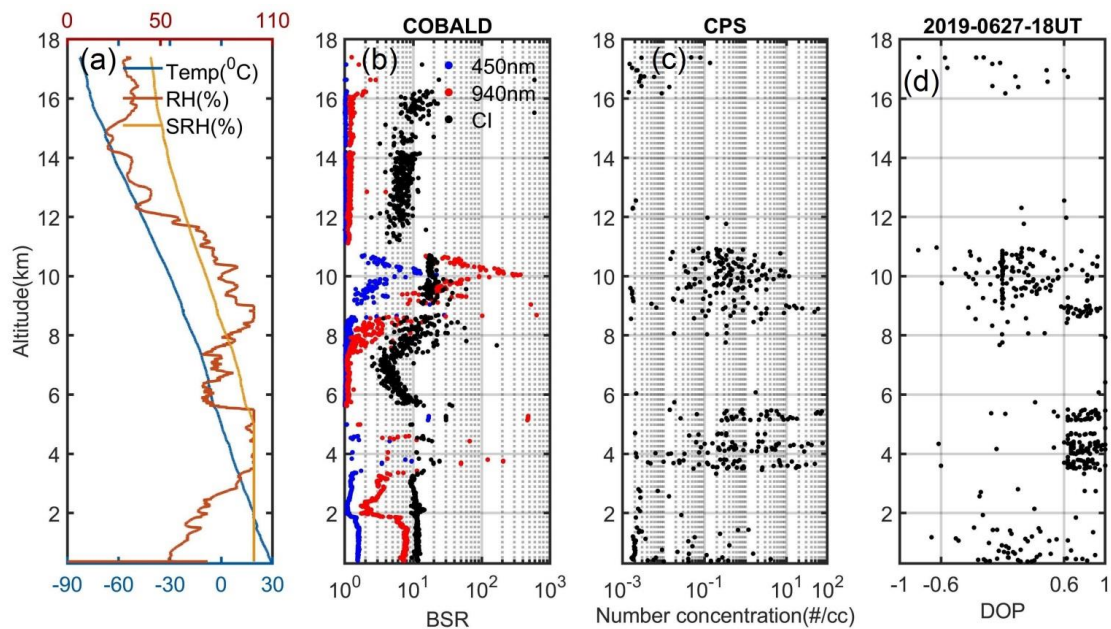
1186
1187 **Figure ~~9~~10**. Combined observations of COBALD and CPS from balloon sounding were held on 27 June 2019 at 2330 LT.
1188 (a) Temperature (T), Relative humidity (RH) and Saturation Relative Humidity (SRH) (b) Backscatter ratio at 455 nm
1189 (blue), 940 nm (red) and Colour Index (Black). (c) Cloud particle number concentration and (d) Degree of polarization
1190 (DOP).
1191
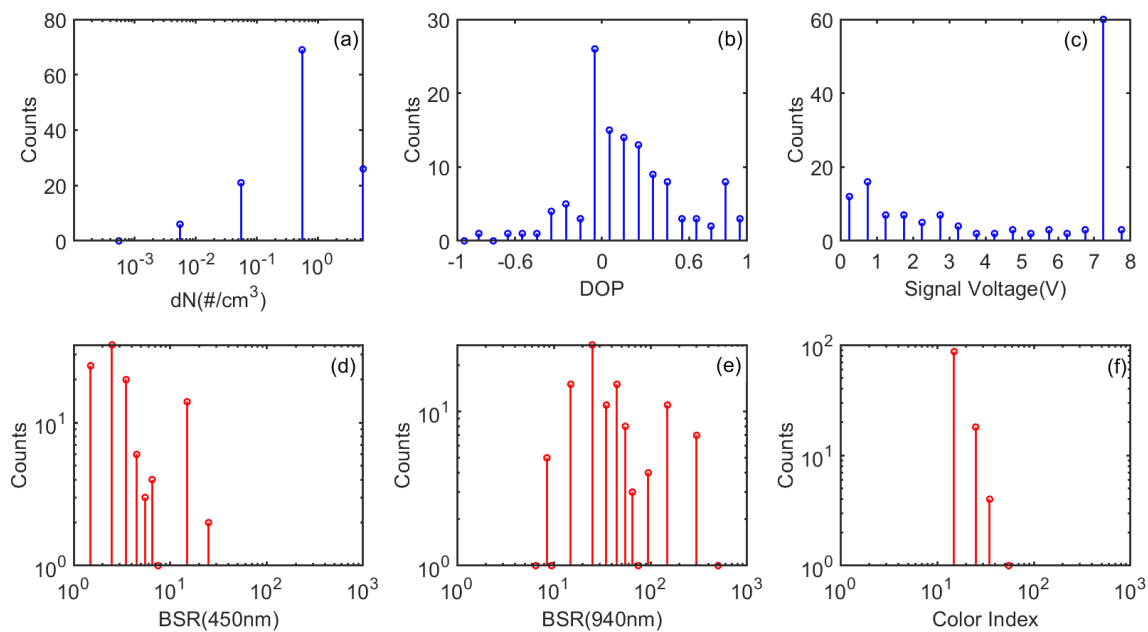
1195 **Figure 110**. Histogram of (a) Droplet number concentration (dN) in #/cc (b) Degree of polarization (DOP) (c) Backscattered
1196 signal (Volts) (d) Backscatter ratio at 455 nm, (e) Backscatter ratio at 940 nm and (f) Colour Index. The top panel shows
1197 the data from CPS and the bottom panel from COBALD for the ice cloud layer between 9 and 11 km from the sounding
1198 held on 27 June 2019.
1199

1200

1201

1202
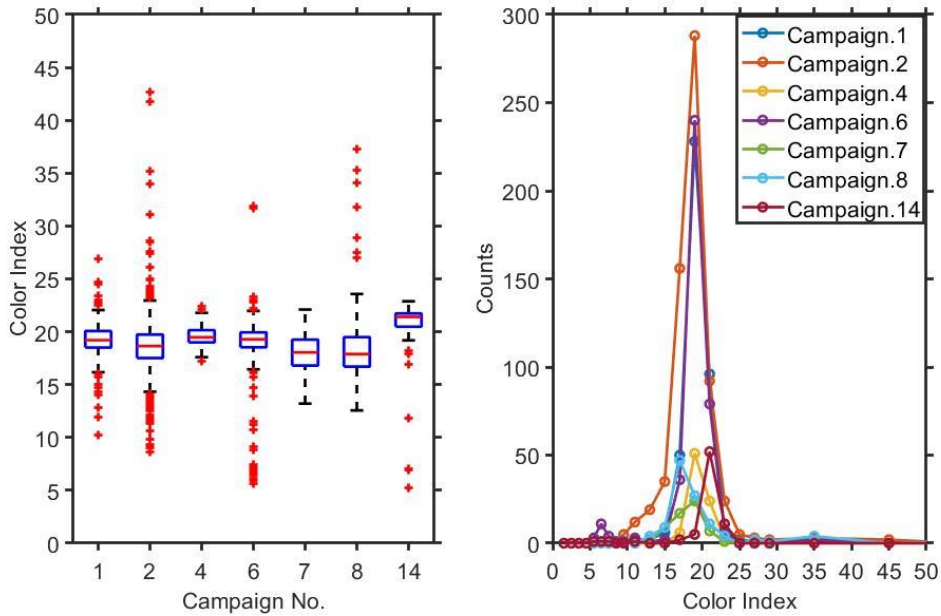
1203
1204 **Figure 1~~2~~1.** (a) The box plot of the Color Index (CI) was observed for the ice clouds found in different campaigns. The
1205 horizontal line in the centre of the box represents the median. The upper and lower edges of the box represent the third
1206 quartile (Q3), and first quartile (Q1) respectively. Similarly, the upper and lower whiskers represent Q3+1.5*(Q3-Q1)
1207 and Q1-1.5*(Q3-Q1). The data points beyond the whiskers (outliers) are shown with red star symbols. (b) The
1208 histogram of the CI values from each campaign. Different colours indicate the data from different campaigns.
1209
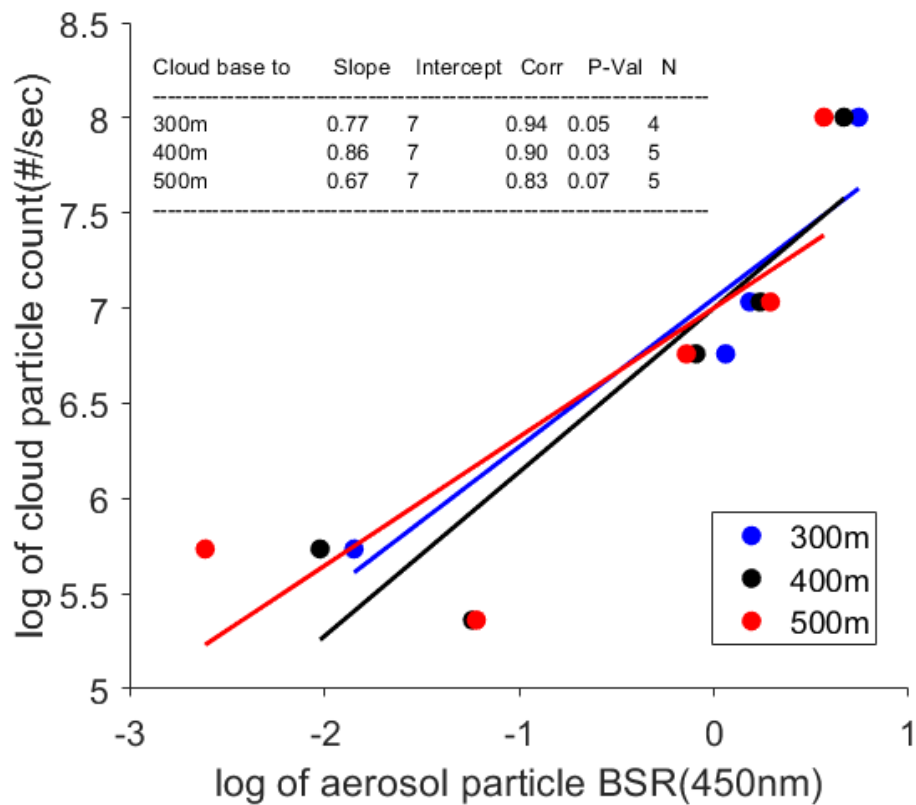
1210

1211 **Figure 1~~3~~2.** Scatter between logarithm values of COBALD median aerosol blue backscatter (x-axis) from 300, 400 and 500

1212 meters below the cloud base and the corresponding CPS median cloud particle count (y-axis) obtained from five balloon

1213 soundings, with a linear fit (different coloured lines). The table inside shows detailed statistics.

1214

1215

1216 *********